J. Fluid Mech. (2023), *vol*. 963, A3, doi:10.1017/jfm.2023.291

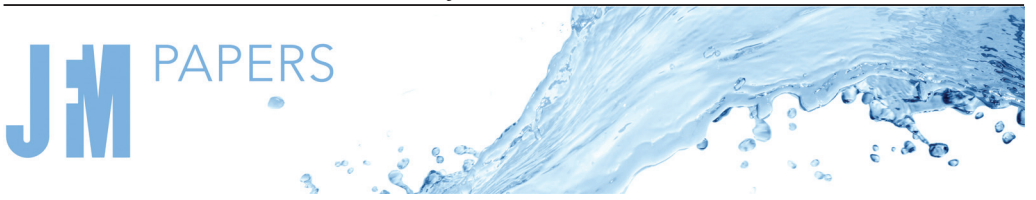

Artificial intelligence control of a low-drag Ahmed body using distributed jet arrays

B.F. Zhang[1],‡, **D.W. Fan**[1],‡ **and Y. Zhou**[1],†

[1]Center for Turbulence Control, Harbin Institute of Technology, Shenzhen 518055, PR China

(Received 6 September 2022; revised 22 March 2023; accepted 31 March 2023)

This work proposes a machine-learning or artificial intelligence (AI) control of a low-drag Ahmed body with a rear slant angle $\varphi = 35°$ with a view to finding strategies for efficient drag reduction (*DR*). The Reynolds number *Re* investigated is 1.7×10^5 based on the square root of the body cross-sectional area. The control system comprises of five independently operated arrays of steady microjets blowing along the edges of the rear window and vertical base, twenty-six pressure taps on the rear end of the body and a controller based on an ant colony algorithm for unsupervised learning of a near-optimal control law. The cost function is designed such that both *DR* and control power input are considered. The learning process of the AI control discovers forcing that produces a *DR* up to 18 %, corresponding to a drag coefficient reduction of 0.06, greatly exceeding any previously reported *DR* for this body. Furthermore, the discovered forcings may provide alternative solutions, i.e. a tremendously increased control efficiency given a small sacrifice in *DR*. Extensive flow measurements performed with and without control indicate significant alterations in the flow structure around the body, such as flow separation over the rear window, recirculation bubbles and C-pillar vortices, which are linked to the pressure rise on the window and base. The physical mechanism for *DR* is unveiled, along with a conceptual model for the altered flow structure under the optimum control or biggest *DR*. This mechanism is further compared with that under the highest control efficiency.

Key words: flow control, machine learning, wakes

1. Introduction

The issues of environmental pollution and global warming highlight the necessity and urgency of searching for new technologies to reduce the aerodynamic drag and hence fuel consumption of road vehicles. With the passive techniques, such as shaping vehicle bodies approaching the optimum, it is active control that may have potential to reduce drag

† Email address for correspondence: yuzhou@hit.edu.cn
‡ Joint first authors.

significantly further. The European motor industry has set a target to reduce actively the aerodynamic drag of vehicles by at least 30 % without restrictions on the comfort, storage and security of passengers (Bruneau *et al.* 2011). Naturally, active control has been recently given great attention in the literature.

The generic Ahmed body (Ahmed, Ramm & Faltin 1984) is widely used as a simplified vehicle model in investigating the drag reduction (*DR*) of vehicles. This model is characterized by a rounded forepart, a straight middle body with a rectangular cross-section and a rear part with a slanted surface, sometimes referred to as the rear window, whose slant angle φ is measured clockwise from the streamwise direction to the slanted surface. The model is divided into high- and low-drag bodies, which correspond to $12.5° < \varphi < 30°$ and $\varphi > 30°$, respectively. The low-drag bodies ($\varphi > 30°$) may represent the commonly used cars such as sport utility vehicles (SUV) and multi-purpose vehicles (MPV), whose rear slant angles are usually larger than 30° (Metka 2013; Edwige *et al.* 2018; Zhou & Zhang 2021). The associated flow is fully separated over the rear window, forming a big recirculation bubble which covers the rear window and most of the base. Meanwhile, one pair of C-pillar vortices are formed along each side edge of the window, whose strength is greatly weakened as compared with that associated with a high-drag Ahmed body. Please refer to Liu, Zhang & Zhou (2021) for more details. Note that the drag coefficient of a square-back Ahmed body ($\varphi = 0°$) is also low, at approximately 0.25. However, the wake of this body is completely different from that of a low-drag body. This flow, where the C-pillar vortices are absent, is characterized by bi-stability (e.g. Grandemange *et al.* 2013), that is, the recirculation region exhibits a random spanwise switch between two preferred reflectional symmetry-breaking positions. This instability has never been observed in the low-drag regime (Liu *et al.* 2021). Therefore, the square-back Ahmed body is often considered to be a special case, not included in the low-drag regime. Please refer to the flow classification in the review article by Zhou & Zhang (2021).

Numerous investigations have been performed on the active *DR* of Ahmed bodies, wherein various techniques are developed, as summarized in tables 1–3. Please refer to Zhou & Zhang (2021) for a recent compendium on this topic. The *DR* in percentage, defined as the ratio of the drag coefficient reduction under control to that in the baseline flow, can clearly reflect the *DR* capability and therefore has been widely used as the major indicator in evaluating the control performance in the literature. Most of previous investigations are focused on the high-drag regime and square-back bodies. For the square-back Ahmed body, Barros *et al.* (2016) deployed four pulsed slot jets with Coanda deflection surfaces along the periphery of the base, achieving a maximum *DR* of 18 %. Haffner *et al.* (2020) investigated the influence of the blowing frequency, intensity, the Reynolds number *Re* and the radius of surface curvature on *DR* using the same actuation technique, and proposed a scaling law for pulsed blowing with the Coanda effect. Lorite-Díez *et al.* (2020*b*) utilized steady slot jets along the four edges of the base and obtained a maximum *DR* of 6 %. Lorite-Díez *et al.* (2020*a*) further deployed steady blowing with different gas media (helium, air and CO_2) near the bottom edge of the base, producing a maximum *DR* of 11 % when helium was used.

There have been a few investigations on the active *DR* of a low-drag Ahmed body (table 3). Park *et al.* (2013) experimentally deployed one array of synthetic jets, issuing through rectangular orifices, along the upper edge of the rear window ($\varphi = 35°$). The jets were directed at 30°, 60° and 90° upward with respect to the streamwise direction. The control led to no *DR* and instead raised the drag by more than 15 %. The synthetic jet arrays were also placed along the two side edges of the rear window, but again no

https://doi.org/10.1017/jfm.2023.291 Published online by Cambridge University Press

Researchers	φ	$Re/10^5$	Actuation technique	Approach	$\Delta C_{D,max}$	DR_{max}
Aubrun *et al.* (2011)	25°	3.1–6.2	Steady blowing at upper edge of rear window	Experimental	0.056	14 %
Bruneau *et al.* (2011)	25°	0.1	Combined steady blowing at upper and two side edges of rear window and suction at mid-height of base	Numerical	0.048	13 %
Boucinha, Weber & Kourta (2011)	25°	2.3	Plasma actuator at upper edge of rear window	Experimental	0.032	8 %
Pernod *et al.* (2011)	25°	1.5–6.1	Pulsed blowing at upper edge of rear window	Experimental	0.025	6 %
Joseph, Amandolese & Aider (2012)	25°	4.5	Pulsed blowing near the end of roof	Experimental	0.026	8 %
Joseph *et al.* (2013)	25°	3.5–6.8	Pulsed blowing near the end of roof	Experimental	0.034	10 %
Kourta & Leclerc (2013)	25°	3.9–6.1	Synthetic jet near the end of roof	Experimental	0.035	9 %
Park *et al.* (2013)	25°	1.4	Synthetic jet at upper edge of rear window	Experimental	0.015	5 %
Metka & Gregory (2015)	25°	4.5	Fluidic oscillator at upper edge of rear window	Experimental	0.033	7 %
Tounsi *et al.* (2016)	25°	3.2–9.6	Synthetic jet at upper edge of rear window	Experimental	0.034	10 %
Shadmani *et al.* (2018)	25°	1.5–2.9	Plasma actuator at upper edge of rear window	Experimental	0.021	7 %
Zhang *et al.* (2018)	25°	1.3–2.0	Combined steady blowing at upper and two side edges of rear window, and upper and lower edges of base	Experimental	0.105	29 %
McNally *et al.* (2019)	25°	6.2	Combined steady blowing at upper edge of rear window and upper edge of base	Experimental	0.051	13 %
Wang, Yang & Zhu (2019)	25°	9.0	Combined pulsed suction at upper edge of rear window and two side edges of base	Numerical	0.081	26 %
Kim, Do & Choi (2020)	25°	1.1–2.3	Plasma actuator at upper edge of rear window	Experimental	0.035	10 %
Liu *et al.* (2021)	25°	1.7	Combined steady blowing at upper and two side edges of rear window, and lower edge of base	Experimental	0.094	26 %

Table 1. Summary of studies on active *DR* of a high-drag Ahmed body in past decade, where the maximum *DR* is denoted by DR_{max}, and the magnitude of the reduced drag coefficient corresponding to the maximum *DR* is denoted by $\Delta C_{D,max}$.

https://doi.org/10.1017/jfm.2023.291 Published online by Cambridge University Press

Researchers	$Re/10^5$	Actuation technique	Approach	$\Delta C_{D,max}$	DR_{max}
Bruneau *et al.* (2010)	0.1	Steady blowing at mid-height of base	Numerical	0.072	23 %
Barros *et al.* (2014)	3.3	Pulsed blowing at four trailing edges of base	Experimental	0.021	7 %
Barros *et al.* (2016)	2.2–4.3	Pulsed blowing with Coanda deflection surface at four trailing edges of base	Experimental	0.053	18 %
Brackston *et al.* (2016)	2.0–3.8	Oscillating flaps at two lateral edges of base	Experimental	0.007	2 %
Li *et al.* (2016)	6.5	Pulsed blowing at two lateral edges of base	Experimental	0.006	2 %
Evstafyeva *et al.* (2017)	0.005	Synthetic jets at four trailing edges of base	Numerical	0.009	3 %
Li *et al.* (2017)	3.3	Pulsed blowing with Coanda deflection surface at four trailing edges of base	Experimental	0.073	24 %
Li *et al.* (2019)	5.4	Pulsed blowing at two lateral edges of base	Experimental	0.019	7 %
Lorite-Díez *et al.* (2019)	1.1	Steady blowing at four trailing edges of base	Experimental	0.011	3 %
Plumejeau *et al.* (2019)	3.3	Pulsed blowing at two lateral edges of base	Experimental	0.009	3 %
Fan *et al.* (2020*a*)	1.7	Pulsed blowing at four trailing edges of base	Experimental	0.037	11 %
Haffner *et al.* (2020)	2.0–3.8	Pulsed blowing with Coanda deflection surface at four trailing edges of base	Experimental	0.03	12 %
Lorite-Díez *et al.* (2020*b*)	1.1	Steady blowing at four trailing edges of base	Experimental	0.022	6 %
Lorite-Díez *et al.* (2020*a*)	0.7	Steady blowing at lower edge of base	Experimental	0.041	11 %
Haffner *et al.* (2021)	5.4	Pulsed blowing with Coanda deflection surface at four trailing edges of base	Experimental	0.035	13 %
Khan *et al.* (2022)	0.8	Steady blowing at the centre of base	Experimental	0.023	6 %

Table 2. Studies on active *DR* for the square-back Ahmed body.

Researchers	φ	$Re/10^5$	Actuation technique	Approach	$\Delta C_{D,max}$	DR_{max}
Jahanmiri & Abbaspour (2011)	35°	9.0	Combined steady suction at upper edge of rear window and blowing at mid-height of base	Experimental	0.013	4 %
Metka (2013)	45°	4.5	Fluidic oscillator at upper edge of rear window	Experimental	—	No DR
Park *et al.* (2013)	35°	1.4	Synthetic jet at upper edge of rear window	Experimental	—	No DR
Edwige *et al.* (2018)	47°	4.9	Pulsed blowing at two lateral edges of base	Numerical	0.004	2 %

Table 3. Active *DR* investigations for the low-drag Ahmed body.

DR was achieved. Metka's (2013) attempt deploying an array of fluidic oscillators along the upper edge of the rear window of an Ahmed body with $\varphi = 45°$ again resulted in a drag increase by 2 %. Jahanmiri & Abbaspour (2011) introduced experimentally and numerically air suction through two rows of holes near the upper edge of the rear window ($\varphi = 45°$), achieving a *DR* of 2 %. They further placed two rows of steady microjets at the mid-height of the base and observed a rise in the static pressure of the flow behind the base. A combination of the two actuations produced a *DR* of 4 %. This is considerably below what has been achieved with the high-drag body. This is to some extent expected. As found by Zhang *et al.* (2018), the key to obtaining a substantial *DR* for a high-drag body lies in the deployment of a combination of three or more independent actuations which may optimally manipulate different coherent structures. As such, the flow structure changes from the high-drag regime, characterized by a separation bubble over the rear window, one pair of counter-rotating longitudinal or C-pillar vortices along two side edges of the slanted surface and two recirculation bubbles behind the vertical base (Ahmed *et al.* 1984), to the low-drag regime characterized by substantially weakened C-pillar vortices and the separation bubble over the rear window joining with the upper recirculation bubble behind the vertical base (e.g. Liu *et al.* 2021). Several issues arise naturally. Could we achieve a substantial *DR* with a reasonable control efficiency even for a low-drag body? Would a combination of multiple independent actuations also work for a low-drag body? If so, how would the flow structure vary or what is the mechanism?

It is a challenge to find the optimal control law when multiple independent actuations are used, especially with many control parameters involved. Artificial intelligence (AI) or machine learning control (MLC) provides a powerful vehicle for improving the effectiveness and efficiency of flow control and hence attracts increasing attention from fluid mechanics researchers. Please refer to Brunton, Noack & Koumoutsakos (2020) for a recent review on this topic. This method searches for the best control law through optimizing the cost function using a regression technique such as genetic programming (e.g. Gautier *et al.* 2015; Parezanović *et al.* 2016; Li *et al.* 2017), artificial neural networks (e.g. Ling, Kurzawski & Templeton 2016; Giannopoulos & Aider 2020; Ren, Hu & Tang 2020) and the explorative gradient method or EGM (e.g. Fan *et al.* 2020*a*; Li *et al.* 2022). Gautier *et al.* (2015) performed a feedback control on the flow separation of a backward-facing step. The actuation was provided by one pulsed slot jet upstream of the upper edge of the step, driven by an online particle image velocimetry (PIV)-based sensing. Genetic programming was deployed, producing a reduction in the reattachment length by 80 %. Li *et al.* (2017) applied pulsed blowing with the Coanda surface along

the four trailing edges of a square-back Ahmed body ($\varphi = 0°$) to reduce the drag. Using the linear genetic programming (LGP) technique, they achieved a maximum *DR* of 24 %. All these investigations have used synchronized actuations where the control parameters are few in number, in general not exceeding three, that is, the momentum coefficient, frequency and duty cycle (e.g. Fan *et al.* 2020*a*). Zhou *et al.* (2020) developed for the first time independent spatially distributed actuators to enhance turbulent jet mixing, where six independently operated unsteady jets were deployed with dozens of independent control parameters. Their learning curve based on the LGP algorithm converged to an optimal control law that led to the finding of a turbulent flow structure, never reported previously, that outperformed significantly all of those classical flow structures well known for jet mixing enhancement. It seems plausible that the AI technique is a natural choice in the search for an optimal control law that may achieve a substantial *DR* for a low-drag Ahmed body given multiple independent actuations. Fan *et al.* (2020*a*) employed experimentally the EGM in their *DR* investigation of a square-back Ahmed body, where four synchronized arrays of pulsed jets were placed around the periphery of the base to manipulate the flow. Their sensitivity analysis of *DR* to control parameters indicated that the control efficiency could be increased by 400 times given a small sacrifice, only 1 %, in *DR*. One naturally wonders whether the AI control could find solutions or forcings that achieve both large *DR* and high control efficiency.

This work sets out to address the issues raised above through a rather extensive experimental investigation on active *DR* of a low-drag Ahmed body with $\varphi = 35°$ using five independent steady jets arranged at every edge of the rear end. An AI system is developed based on the ant colony algorithm (ACA) to search for the optimum control strategies of these independent actuators. Experimental details are provided in § 2. The deployed AI system is described in § 3. The results are presented in § 4, including the base flow, the effects of individual actuations on the drag, the AI-based optimization for the combined actuations and the underlying flow physics or *DR* mechanisms, the sensitivity analysis on each control parameter and the control efficiency. This work is concluded in § 5.

2. Experimental details

2.1. *Experimental set-up*

Experiments were performed in a closed circuit wind tunnel with a 5.6 m long rectangular test section (1.0 m high and 0.8 m wide). The flow non-uniformity is 0.1 % and the longitudinal turbulence intensity is less than 0.4 % in the test section for the given experimental conditions. Figure 1(*a*) schematically shows the experimental set-up. A flat plate of 2.6 m × 0.78 m × 0.015 m was installed horizontally, 0.1 m above the floor of the test section as a raised floor to control the boundary layer thickness. Following the design of Narasimha & Prasad (1994), its leading edge was shaped to a clipper-built curve to avoid flow separation. The plate leading edge was placed 2 m downstream of the exit plane of the tunnel contraction.

The vehicle model was a standard 1/2-scaled Ahmed body following Ahmed *et al.* (1984) with a rear slant surface angle (φ) of 35°, whose overall length (L), width (W) and height (H) were 0.522 m, 0.1945 m and 0.144 m (figure 1*b*,*c*), respectively. The model was supported by four hollow cylindrical struts of 15 mm diameter, and the clearance between the model underside and the raised floor was 25 mm. Its front end was 0.3 m downstream of the floor leading edge, where the boundary thickness was approximately 4 mm at a free-stream velocity (U_∞) of 12 m s^{-1}. The blockage ratio of the model to the test section was approximately 3.9 %. The coordinate system (x, y, z) is defined in

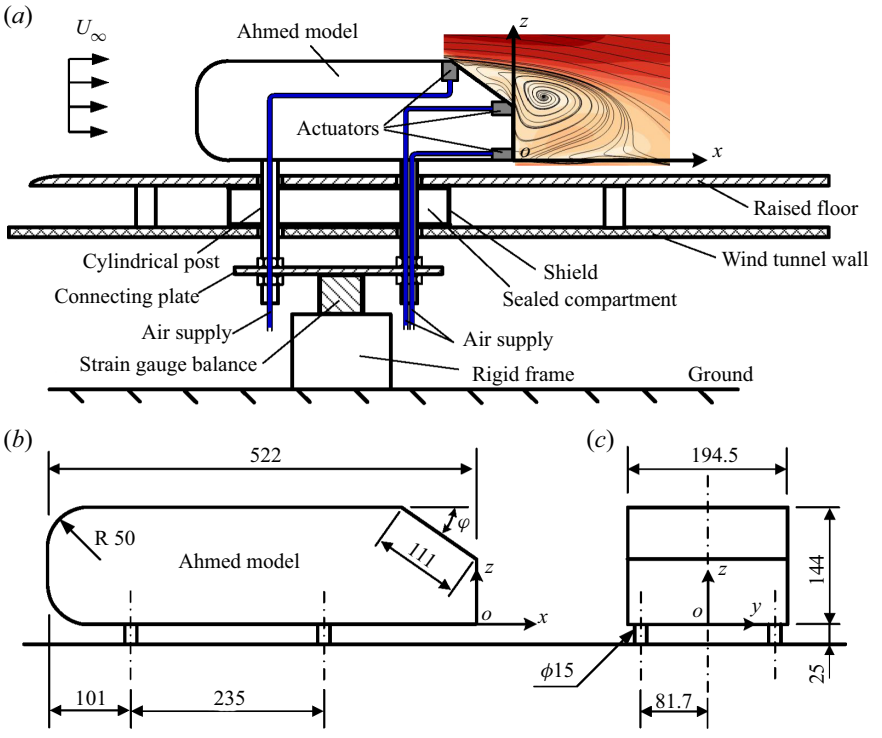

Figure 1. (*a*) Schematic of experimental arrangement. (*b*) Side and (*c*) back views and dimensions of a 1/2 scaled Ahmed body. The length unit is mm.

figure 1(*b*,*c*). The instantaneous velocity components along the x, y and z directions are defined as U, V and W, respectively, which can be decomposed as $U = \bar{U} + u$, $V = \bar{V} + v$ and $W = \bar{W} + w$, where the overbar denotes time averaging, and u, v and w are fluctuating velocities. The superscript asterisk denotes normalization by the square root of the model frontal area $\sqrt{A}(= 0.167$ m) and/or U_∞; for example, $f^* = f\sqrt{A}/U_\infty$, $\omega_x^* = \omega_x\sqrt{A}/U_\infty$, $\omega_y^* = \omega_y\sqrt{A}/U_\infty$ and $\omega_z^* = \omega_z\sqrt{A}/U_\infty$, where f is frequency, ω_x, ω_y and ω_z are the instantaneous vorticity components along the x, y and z directions, respectively.

Liu *et al.* (2021) carried out a relatively thorough investigation on the flow structures around this body and proposed a conceptual model of the flow structures. Unlike the well-known classical flow structure model developed by Ahmed *et al.* (1984), which is constructed based on time-averaged data, Liu *et al.*'s (2021) model embraces both steady and unsteady coherent structures around the body and even the predominant frequencies of the unsteady structures. Based on this model, five different actuations based on constant blowing, referred to as C_1, C_2, C_3, C_4 and C_5 (figure 2*a*), were deployed. C_1, C_3 and C_5 are three arrays of microjets along the upper and lower edges of the slanted surface and the lower edge of the base, respectively, each array consisting of 45 circular orifices of 1 mm diameter; C_2 and C_4 each comprise two microjet arrays, arranged along the two side edges of the rear window and the vertical base, respectively, each array includes 28 orifices for C_2 and 15 for C_4. The separation between two neighbouring orifices is the same, 2 mm, for all actuations. The blowing angle θ_{Ci} of C_i ($i = 1, 2, \ldots, 5$) may change via replacing the actuator, each fabricated with a different θ_{Ci}. Three blowing angles of 0°, 55°and 120°

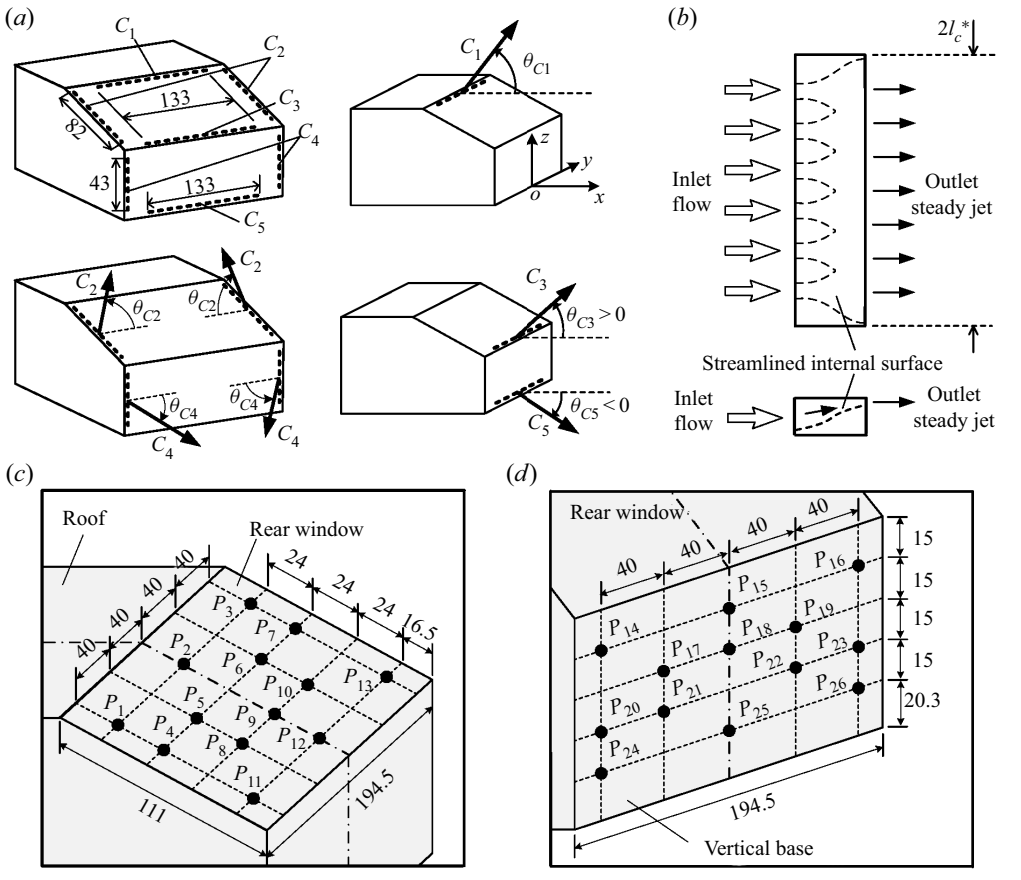

Figure 2. (*a*) Arrangement of actuations on the rear window and the vertical base of the Ahmed body and the definitions of the blowing angles, where θ_{C3} and θ_{C5} are positive and negative, respectively. (*b*) Top and side views of the chamber. Measurement locations of surface pressure on (*c*) the rear window and (*d*) the vertical base. The length unit is mm.

were tested for *DR* for each of C_1 and C_3, and angles of 30°, 90° and 150° for each of C_2 and C_4; C_5 was examined at $\theta_{C5} = -45°$, 0° and 45°.

Each array of microjets is associated with a separate chamber (figure 2*b*), embedded in the model. The chamber is connected to supply air via a flexible tube through the hollow strut of the model. The tube is hanging vertically downward from the model before reaching the ground, so that the resultant horizontal force between the tube and the ground is negligibly small. The chamber inlet consists of 6 equally separated holes of 8 mm diameter for C_1, C_3 and C_5, and 3 and 2 holes for C_2 and C_4, respectively. Air flows into the chamber along streamlined diverging passages before reaching the outlet, which act to minimize the non-uniformity of the microjets through the orifices. The flow rate through the chamber is measured and controlled using a mass flow controller (Flow Method FL-805) with a measuring range of 0–2001 min^{-1} and an uncertainty of $\pm 21\,\text{min}^{-1}$. The blowing ratio BR^{Ci} is defined by

$$BR^{Ci} = \frac{V_{Ci}}{U_\infty}, \tag{2.1}$$

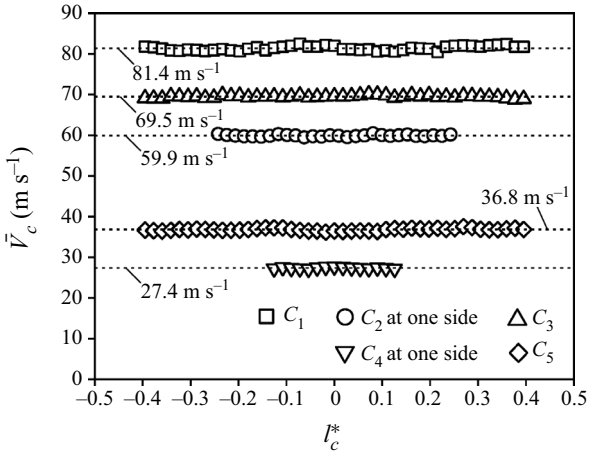

Figure 3. Distributions of $\overline{V_c}$ along each microjet array measured at 1 mm above the centre of the jet exit: C_1 ($\theta_{C1} = 55°$), $C_\mu^{C1} = 0.081$; C_2 ($\theta_{C2} = 90°$), $C_\mu^{C2} = 0.051$; C_3 ($\theta_{C3} = 55°$), $C_\mu^{C3} = 0.056$; C_4 ($\theta_{C4} = 90°$), $C_\mu^{C4} = 0.006$; C_5 ($\theta_{C5} = 0°$), $C_\mu^{C5} = 0.016$.

where V_{Ci} is the exit velocity of a microjet. Figure 3 presents the distributions of the time-averaged centreline velocity $\overline{V_c}$ along the jet exit for each of the five actuations (C_1, C_2, C_3, C_4 and C_5). This velocity was measured using a Pitot static tube connected to an electronic manometer (Furness FCO560) 1 mm downstream of the jet exit. The value of $\overline{V_c}$ exhibits a very small variation, $<2\,\%$ of $\overline{V_c}$, from one microjet to another, irrespective of C_i ($i = 1, 2, \ldots, 5$).

2.2. *Flow measurements*

A single hot-wire was placed along the y-direction to measure the velocity fluctuations u_{xz} in the (x, z) plane to detect the predominant frequencies in the wake. The sensing element was a tungsten wire 5 μm in diameter and approximately 1 mm in length. The wire was operated on a constant temperature circuit (Dantec Streamline) at an overheat ratio of 1.8. The signal from the wire was offset, amplified and low-pass filtered at a cutoff frequency of 1.0 kHz, and digitized at a sampling frequency f_s of 6 kHz using a 16-bit A/D converter (NI PCI-6143). Hot-wire measurements were performed at $x^* = 0.8$, $y^* = 0$ and $z^* = 0$. The sampling duration was 60 s, producing a total of 3.6×10^5 data for each record. At least three records were obtained for each test configuration. A fast Fourier transform (FFT) algorithm was used to calculate the power spectral density function E_u of u_{xz}, which is normalized by the variance of u_{xz} so that its integration over the entire frequency range is unity. The FFT window size N_w was 4096. The frequency resolution Δf in the spectral analysis depends on f_s and N_w, *viz.* $\Delta f = f_s/N_w$ (e.g. Zhou *et al.* 2012) $= 1.46$ Hz.

A LaVision planar PIV system was used to measure the wake of the Ahmed model. The model surface, raised floor and tunnel working section walls were all painted black to minimize laser reflection. The flow was seeded with Di-Ethyl-Hexyl-Sebacat tracer particles approximately 1 μm in diameter. Flow illumination was provided by two standard pulsed laser sources (Vlite-200) of 532 nm wavelength, each with a maximum energy output of 200 mJ per pulse. Each laser pulse lasted for 0.01 μs. One charge-coupled device (CCD) camera (Imager pro HS4M, 4-megapixel sensors, 2016×2016 pixels resolution) was used to capture particle images. Synchronization between image taking and flow

illumination was provided by the LaVision timer box. The PIV measurements were performed in the (x, z) planes at $y^* = 0$ (symmetry plane) and 0.36, the (x, y) plane of $z^* = 0.24$ and 0.67 and the (y, z) plane at $x^* = -0.09$ and 0.43. The PIV images covered an area of $x^* = -0.95$ to 1.5 and $z^* = -0.74$ to 1.71 in the (x, z) planes, $x^* = -0.61$ to 1.74 and $y^* = -1.12$ to 1.23 in the (x, y) planes and $y^* = -0.92$ to 0.91 and $z^* = -0.23$ to 1.6 in the (y, z) planes. The image magnifications in both directions of each plane were identical, approximately 203, 195 and 152 μm pixel^{-1} in the (x, z), (x, y) and (y, z) planes, respectively. The intervals between two successive pulses were 90 μs, 80 μs and 20 μs for measurements in the (x, z), (x, y) and (y, z) planes, respectively. In processing the PIV images, the adaptive PIV method was used with a minimum interrogation area size of 32×32 pixels and a maximum size of 64×64 pixels. The grid step size of 16×16 pixels produced 126×126 in-plane velocity vectors and the same number of vorticity data points ω_x, ω_y or ω_z.

Following Zhang *et al.* (2018) and Liu *et al.* (2021), the uncertainty of PIV measurements was evaluated based on image matching analysis. This approach identifies particle image pairs in two successive exposures according to the measured displacement vectors, and evaluates the residual distance or particle disparity between the particle image pairs, which dictates the uncertainty of velocity measurements. Further details of this technique can be found in Sciacchitano, Wieneke & Scarano (2013). In the (x, z) planes of $y^* = 0$ and 0.36, the root-mean-square (r.m.s.) value of the disparity was found to be approximately 0.05 pixel in both the x and z directions, resulting in the uncertainties, σ_U and σ_W, in U and W of $0.7\,\%U_\infty$. The r.m.s. values of the disparity were found to be 0.05 pixel in the (x, y) planes of $z^* = 0.24$ and 0.67, and 0.04 pixel in the (y, z) planes of $x^* = -0.09$ and 0.43. The uncertainties (σ_U and σ_V) of U and V in the (x, y) planes are estimated to be approximately $0.9\,\%U_\infty$, and those (σ_V and σ_W) in the (y, z) planes are approximately $2\,\%U_\infty$. A total of 1800 images were captured for each test run, with a trigger rate of 15 Hz in the double frame mode. The percentage variations of $\bar{U}^*$, $\bar{V}^*$, $\bar{W}^*$, $\bar{\omega}_x^*$, $\bar{\omega}_y^*$ or $\bar{\omega}_z^*$ converge with an increasing number of images to less than ± 1 % once the image number exceeds 1200, irrespective of the measurement plane or trigger rate. As such, 1800 images are considered to be adequate for capturing the mean and fluctuating flow fields.

2.3. *Aerodynamic drag and surface pressure measurements*

Time-averaged aerodynamic drag was measured using a six-component force balance (China Academy of Aerospace Aerodynamics, HGDDS-80), which is accurate to 0.01 N. The balance was mounted on a rigid frame fixed directly onto the ground surface in order to minimize the effect of wind tunnel vibration on measurements (figure 1*a*). The test model was rigidly mounted on the balance via the four hollow cylindrical posts 280 mm in height, which were fixed to a horizontal connecting plate that was screwed onto the balance. The posts were isolated from the raised floor and the wind tunnel, and were enclosed by a sealed compartment between the raised floor and the bottom wall of the tunnel test section, to avoid the force transmission and the effect of aerodynamic forces resulting from the gap flow on measurements. Without sealing the compartment, the drag force induced by the flow between the raised floor and the bottom wall on each cylindrical support is estimated to be approximately 0.22 N, approximately 18 % of the drag on the Ahmed body, given a flow velocity of 15 m s^{-1}. The sampling frequency was 1 kHz for the drag force measurement with a duration of 60 sec, producing a total of 6×10^4 samples for each record. At least three records were collected for each test configuration.

Following Littlewood & Passmore (2012), the aerodynamic drag F_D is given by the force-balance-measured drag F_x subtracted by the thrust force F_j induced by the blowing jets, *viz.*

$$F_D = F_x - F_j, \tag{2.2}$$

where F_j was obtained at $U_\infty = 0\ \mathrm{m\ s^{-1}}$. The drag coefficient C_D is calculated by

$$C_D = \frac{F_D}{0.5\ \rho\ U_\infty^2 A}. \tag{2.3}$$

The drag coefficient variation ΔC_D is defined by

$$\Delta C_D = \frac{C_D - C_{D0}}{C_{D0}}, \tag{2.4}$$

where C_{D0} is the drag coefficient of the model in the absence of control.

The pressures on the slanted surface and the vertical base were monitored from twenty-six pressure taps (figure 2*c*,*d*), which were connected to an electronic pressure scanner (a PSI DTC Initium system) using the plastic tubes of 1 mm inner diameter. The scanner was placed inside the test model to minimize the length of the tubes connected to each tap and hence to limit the filtering effect of tubing in pressure measurements (Grandemange *et al.* 2013). The measurement uncertainty is estimated to be ± 1 Pa. At least three test runs were conducted for each flow condition. The sampling duration is 60 s, with a f_s of 650 Hz, for pressure measurements. The instantaneous pressure coefficient C_{pi} is given by

$$C_{pi} = \frac{p_i - p_0}{0.5\rho U_\infty^2}, \quad i \in \{1, 2, \ldots, 26\}, \tag{2.5}$$

where p_i is the instantaneous local pressure and p_0 is the free-stream static pressure ($=45$ Pa at $U_\infty = 15\ \mathrm{m\ s^{-1}}$) measured at $x^* = -4.9$, $y^* = 0$ and $z^* = 3.1$ above the leading edge of the raised floor. The change $\Delta\overline{C_{pi}}$ of the time-averaged local pressure coefficient is given by

$$\Delta\overline{C_{pi}} = \frac{\overline{C_{pi}} - \overline{C_{pi0}}}{|\overline{C_{pi0}}|}, \tag{2.6}$$

where C_{pi0} is the instantaneous pressure coefficient in the baseline flow. The spatially averaged pressure coefficients on the rear window ($\langle\overline{C_p}\rangle_r$) and the vertical base ($\langle\overline{C_p}\rangle_b$) are calculated by

$$\langle\overline{C_p}\rangle_r = \frac{\sum_{i=1}^{13} \overline{C_{pi}}}{13}, \tag{2.7}$$

and

$$\langle\overline{C_p}\rangle_b = \frac{\sum_{i=14}^{26} \overline{C_{pi}}}{13}. \tag{2.8}$$

The contribution of $\langle\overline{C_p}\rangle_r$ and $\langle\overline{C_p}\rangle_b$ to the force along the drag direction can be expressed by

$$\langle\overline{C_p}\rangle = \frac{\langle\overline{C_p}\rangle_r\ \sin(\varphi) + \langle\overline{C_p}\rangle_b}{2}. \tag{2.9}$$

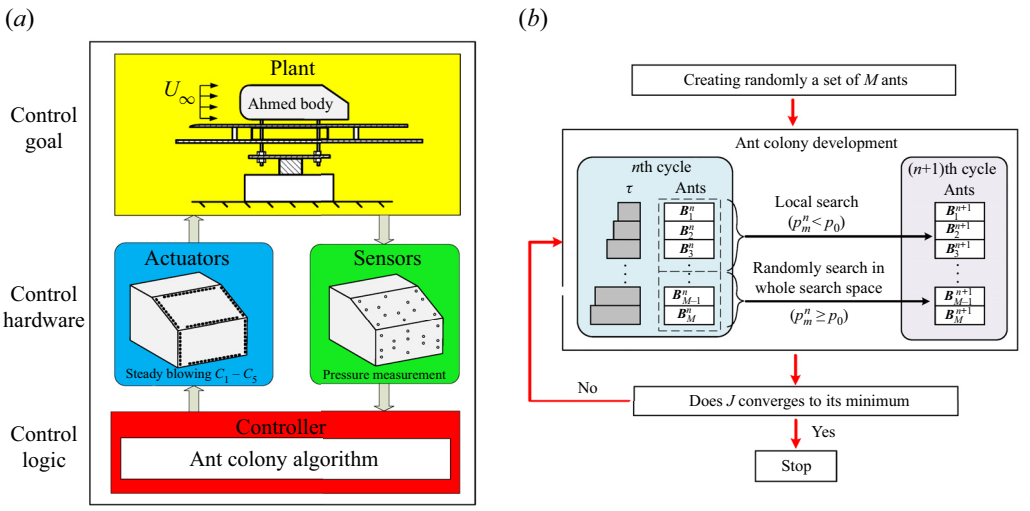

Figure 4. (*a*) Sketch of the principle of the AI control system, which comprises the plant, sensors, actuators and an ACA controller. (*b*) Schematic of ant colony optimization algorithm.

Then, the change of $\langle\overline{C_p}\rangle$ is given by

$$\Delta\langle\overline{C_p}\rangle = \frac{\langle\overline{C_p}\rangle - \langle\overline{C_{p0}}\rangle}{|\langle\overline{C_{p0}}\rangle|}, \tag{2.10}$$

where $\langle\overline{C_{p0}}\rangle$ is the effective spatially averaged pressure coefficient in the absence of control. The negative or positive sign of $\Delta\langle\overline{C_p}\rangle$ represents a drop or rise in pressure.

The aerodynamic drag measurements were carried out at U_∞ from 7.5 to 24 m s^{-1}, corresponding to the Re range of (0.9–2.7) $\times 10^5$ based on $\sqrt{A}$ and U_∞, and all other measurements were performed at $U_\infty = 15$ m s^{-1} ($Re = 1.7 \times 10^5$).

3. AI Control based on ACA

3.1. *AI control system and cost function design*

The AI control system sketched in figure 4(*a*) consists of a plant, a sensing unit (pressure taps), an execution unit and a control logic/controller, as in Zhou *et al.* (2020). The control logic provides the execution unit with instructions or commands, and the latter, i.e. the independently operated microjet arrays, then executes, which manipulates the control plant (the flow around the Ahmed body). The real-time control command is generated by a National Instrument PXIe-6356 multifunction *I/O* device, connected to a computer. A LabVIEW Real-Time module is used to execute the command. The sensing unit monitors the plant output and processes the information from the pressure taps, based on which a decision will be made on whether the control goal has been achieved. If yes, stop; otherwise, continue the search for the optimal control parameters. The execution hardware and control logic are intimately interwoven, facilitating achieving of the control goal of the plant. Before introducing the control logic in § 3.2, we discuss the set-up of the control goal, i.e. the design of the cost function J.

Aiming to find efficient control strategies, which may achieve a substantial DR at small expenses, i.e. small control power input, we define J by

$$J = -\langle\overline{C_p}\rangle + \beta_p, \tag{3.1}$$

where $-\langle\overline{C_p}\rangle$ provides a measure for the estimate of drag (Li *et al.* 2017; Fan *et al.* 2020*a*) and β_p is the penalization term connected to the control power input, given by

$$\beta_p \;=\; \alpha \sum_{i=1}^{5} (BR^{Ci})^3. \tag{3.2}$$

In (3.2), α is a weighting factor. Following the energy input analyses by Wassen & Thiele (2010), Barros *et al.* (2016) and Zhang *et al.* (2018), the power input of C_i ($i = 1, 2, \ldots, 5$) may be calculated by

$$P_{Ci} = 0.5 N_{Ci} \rho A_{Ci} U_\infty^3 (BR^{Ci})^3, \tag{3.3}$$

where N_{Ci} is the number of microjets, and A_{Ci} is the exit area of a microjet. The choice of α is twofold. First, α is such that the penalization term plays an appreciable role in control; second, α cannot be too large to dominate J (Raibaudo *et al.* 2020). The present α is set at 0.00002 so that the penalization term is between 0.04 % and 9 % of $-\langle\overline{C_{p0}}\rangle$ when BR^{Ci} increases from 1 to 6 for each actuation. The variation in J is given by

$$\Delta J = \frac{J - J_0}{J_0}, \tag{3.4}$$

where J_0 is the cost for the baseline flow.

3.2. *Optimization algorithm based on ACA*

In the present control system, there are five control parameters, i.e. BR^{C1}, BR^{C2}, BR^{C3}, BR^{C4} and BR^{C5}, to be optimized. It becomes challenge for conventional optimization techniques once the number of control parameters exceeds three; for instance, the extremum seeking method based on extended Kalman filter could be applied to at most three control parameters (Fan, Zhou & Noack 2020*b*). On the other hand, the AI control may get around this difficulty and may find the global optimum solution even when the number of control parameters is rather large, as demonstrated by Zhou *et al.* (2020).

The ACA is presently used. Inspired by the behaviour of ant colonies in nature, Dorigo *et al.* (1991) proposed an approach for solving hard combinatorial or discrete problems. In their work, the well-known travelling salesman problem was used as an application example, and the ACA was found to be effective in finding out the optimal or shortest tour. The ACA uses many interacting agents, called artificial ants mimicking the real ones mediated by pheromone trails, and an algorithm based on positive feedback for exploring rapidly the optimal solution. Liao *et al.* (2014) developed a unified framework of ACA, in which the ants in each cycle are divided into two groups, one whose costs are below a threshold, performing a local search near the best ant, and the other executing a global search in the entire parameter space. This method is demonstrated to be efficient in finding the global optimum solutions, when applied to more than 20 benchmark multimodal functions, without being trapped in local minima. They obtained the global extremum for every benchmark function with faster speed and higher accuracy as compared with conventional ACA methods (Dorigo *et al.* 1991; Socha & Dorigo 2008). This ACA is implemented presently for the first time as an algorithm of MLC in order to find the best control strategy for the DR of an Ahmed body wake, and is briefly introduced below.

The vector $\boldsymbol{B}=[b_1,\ b_2,\ \ldots,\ b_5]^{\mathrm{T}}$ comprises all actuation commands or analogue voltages, where the superscript 'T' denotes the transpose and b_i $(i=1,\ 2,\ 3,\ 4$ or $5)$ regulates the mass flow controller for C_i (figure 4*a*). Then

$$\boldsymbol{B}=\boldsymbol{K}(\boldsymbol{BR}), \tag{3.5}$$

where $\boldsymbol{BR}=[BR^{C1},\ BR^{C2},\ \ldots,\ BR^{C5}]^{\mathrm{T}}$ is referred to as the control law of the combined actuations in this paper and $\boldsymbol{K}$ is the vector function that transforms $\boldsymbol{BR}$ to the control signals of the mass flow controllers. The optimization process searches for a law of form (3.5) that minimizes the cost:

$$\boldsymbol{K_{opt}}=\arg\min_{\boldsymbol{K}}\ J[\boldsymbol{K}(\boldsymbol{BR})]. \tag{3.6}$$

The regression problem is to optimize mapping from five inputs (BR^{C1}, BR^{C2}, $\ldots$, BR^{C5}) to a single output signal J and the optimizing process is schematically shown in figure 4(*b*), described briefly below:

Step 1: the process is initialized with a set of $M=100$ randomly generated $\boldsymbol{BR_m^n}$, $m=1,\ldots,M$, also called ants, for the first cycle of ACA ($n=1$). Here, the superscripts 'n' and 'm' denote the cycle number and the mth control command of each cycle.

Step 2: each 'm' is experimentally tested for 25 s to yield the measured cost J_m^n. The pheromone (τ_m^n) is given by

$$\tau_m^n=(1-e_v)\tau_m^{n-1}+J_m^n,\quad (n=1,\ldots,N), \tag{3.7}$$

where e_v is the evaporation rate and is set to 0.9, and N is the total number of cycles. The value of τ_m^0 is zero. Then, the ants are renumbered in order of the pheromone values, $\tau_1^n<\tau_2^n<\cdots<\tau_M^n$.

Step 3: the ants are sorted into two groups, one performing a local search, and the other regenerated randomly in the entire search space. The transition probability (P_m^n) for the local search is written as

$$P_m^n=\begin{cases}1 & p_m^n\ <\ p_0\\ 0 & p_m^n\ \geq\ p_0\end{cases}, \tag{3.8}$$

where p_0 is a threshold, which affects largely the ratio of ants that perform local or global searches. A right choice of p_0 may raise the efficiency of the global searching of the ACA, ensuring a relatively large number of ants to be generated randomly in the entire search space (or global searching). Otherwise, most ants may get engaged in local searching. The p_0 is presently chosen to be 0.2 after a trial-and-error process. The p_m^n is a variation in τ_m^n relative to τ_1^n, *viz.*

$$p_m^n\ =\ \frac{\tau_m^n-\tau_1^n}{\tau_1^n}. \tag{3.9}$$

The ant conducting the local search is determined by

$$\boldsymbol{BR_m^{n+1}}=\boldsymbol{BR_m^n}+\frac{1}{2n}\boldsymbol{R_a},\quad \boldsymbol{R_a}=[r_1,r_2,\ldots,r_5]^{\mathrm{T}}, \tag{3.10}$$

where r_i $(i=1,\ 2,\ \ldots,\ 5)$ can be expressed by

$$r_i=2S_i[\mathrm{rand}(0,\ 1)-0.5], \tag{3.11}$$

and S_i denotes the maximum BR^{Ci} for C_i.

Step 4: next cycle starts with step 2 until the cost is converged to its minimum.

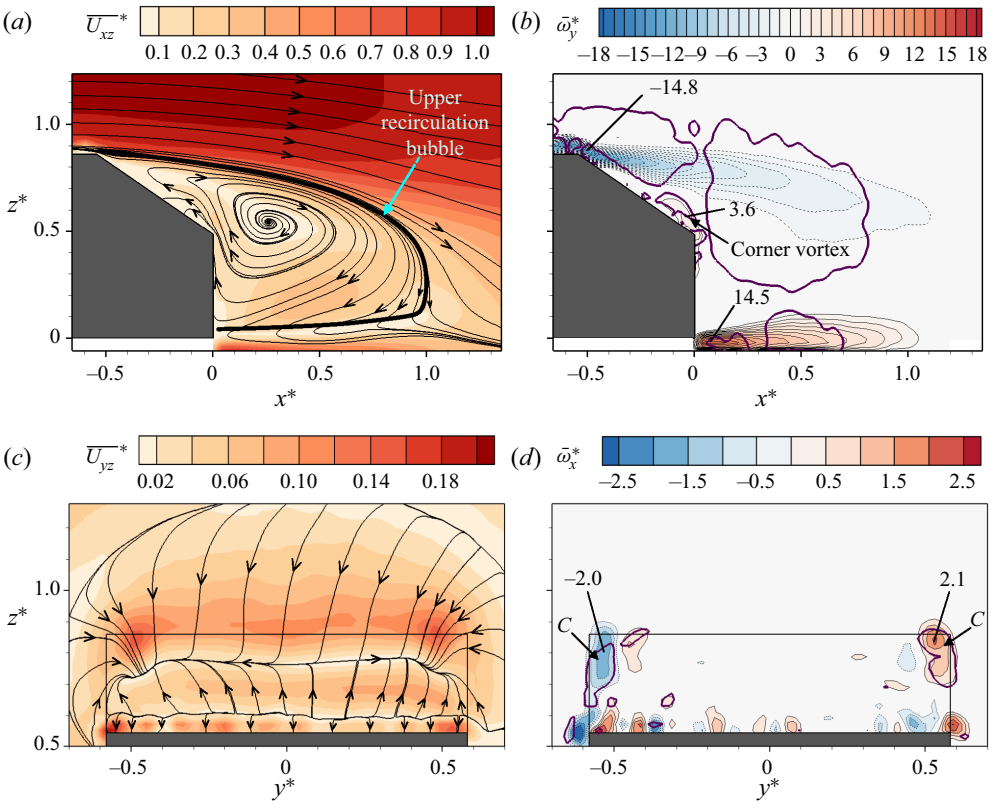

Figure 5. (*a*) Time-averaged streamlines superimposed with the contours of velocity magnitude $\overline{U_{xz}}^*$ and (*b*) $\bar{\omega}_y^*$-contours in the symmetry plane (vorticity contour interval = 1). (*c*) Time-averaged streamlines superimposed with the contours of velocity magnitude $\overline{U_{yz}}^*$ and (*d*) $\bar{\omega}_x^*$-contours in the (y, z) plane of $x^* = -0.09$ (vorticity contour interval = 0.5). Thick purple closed contours correspond to the time-averaged swirling strength $\overline{\lambda_{ci}^2}^* = 0.1$ and 0.02 in (*b*) and (*d*), respectively. Flow is unforced.

4. Results and discussion

4.1. *Base flow characterization*

The base flow of the Ahmed body is first documented. Its drag coefficient C_{D0} drops from 0.36 to 0.29 with increasing Re from 0.9×10^5 to 2.7×10^5. The uncertainty in C_{D0}, given by $|C_{D0} - \overline{\overline{C_{D0}}}|$, where the double overbar denotes averaging over three test runs (Bidkar *et al.* 2014), is estimated to be between 0.0005 and 0.004, one order of magnitude smaller than the drop (0.07) in C_{D0}. The measured C_{D0} and its variation agree well with previous reports on an Ahmed body with $\varphi = 35°$ by Ahmed, Ramm & Faltin (1984), Guilmineau (2008), Meile *et al.* (2016) and Liu *et al.* (2021), who observed a decline in C_{D0} from 0.32 to 0.26 from $Re = 1.7 \times 10^5$ to 1.4×10^6.

Figure 5(*a*) presents the time-averaged sectional streamlines superimposed over the in-plane velocity magnitude $\overline{U_{xz}}^*$ in the symmetry plane of the wake. Hereinafter, the sectional streamlines are referred to as streamlines for simplicity. Flow separates from the upper edge of the rear window and the lower edge of the vertical base and then rolls up, forming two recirculation bubbles, one above the other (e.g. Lienhart & Becker 2003; Liu *et al.* 2021). The upper bubble is much bigger than the lower one, covering both the

rear window and most of the upper part of the base, which is highlighted by the thick solid contour in figure 5(*a*). The streamlines may allow us to determine the length of the recirculation bubbles, defined by the maximum longitudinal bubble length of $\bar{U} \leq 0$ (e.g. Zhang, Zhou & To 2015). The length (l^*_{u0}) of the upper recirculation bubble is approximately 0.98. The lower bubble is hardly discernible in the streamlines, probably because of a jittering in this bubble during time averaging (Liu *et al.* 2021). Within the upper bubble, the upwash flow near the base separated from the upper edge of the base and then rolled up under the pressure difference between the flow at the base and that over the rear window, generating a corner vortex. This vortex accounts for the anti-clockwise rotation of streamlines near the lower edge of the slanted surface (figure 5*a*).

The vortex definition proposed by Zhou *et al.* (1999), which is briefly introduced below, is adopted for the identification of vortices from the vorticity data. A vortex core is a region where the velocity gradient tensor $\nabla \boldsymbol{U}$ has complex eigenvalues (Chong, Perry & Cantwell 1990). Then, $\nabla \boldsymbol{U}$ may be written as

$$\nabla \boldsymbol{U} = \begin{bmatrix} \boldsymbol{v}_r & \boldsymbol{v}_{cr} & \boldsymbol{v}_{ci} \end{bmatrix} \begin{bmatrix} \lambda_r & & \\ & \lambda_{cr} & \lambda_{ci} \\ & -\lambda_{ci} & -\lambda_{cr} \end{bmatrix} \begin{bmatrix} \boldsymbol{v}_r & \boldsymbol{v}_{cr} & \boldsymbol{v}_{ci} \end{bmatrix}^{-1}, \tag{4.1}$$

where λ_r is the real eigenvalue with a corresponding eigenvector $\boldsymbol{v}_r$, and $\lambda_{cr} \pm \lambda_{ci}\boldsymbol{i}$ is a conjugate pair of the complex eigenvalues with eigenvectors $\boldsymbol{v}_{cr} \pm \boldsymbol{v}_{ci}\boldsymbol{i}$. The local flow is either stretched or compressed along the axis $\boldsymbol{v}_r$, while swirling in the plane determined by vectors $\boldsymbol{v}_{cr}$ and $\boldsymbol{v}_{ci}$. The local swirling strength of the vortex is given by the imaginary part of the complex eigenvalue pair λ_{ci}. This method is independent of the reference frame and would not detect regions containing significant vorticity such as shear layers but no local swirling motion. A vortical motion is identified if λ^{2*}_{ci} is larger than a threshold, approximately 3 % of the maximum λ^{2*}_{ci}, which is 0.100 in the (x, z) planes of $y^* = 0$ and 0.36 and the (x, y) planes of $z^* = 0.24$ and 0.67, and 0.020 and 0.001 in the (y, z) planes of $x^* = -0.09$ and 0.43, respectively.

The $\bar{\omega}^*_y$ contours in the symmetry plane (figure 5*b*) display an upper negative-signed concentration and a lower positive-signed concentration, both spatially coinciding with purple-coloured thick solid contours of $\lambda^{2*}_{ci} = 0.1$. Obviously, the two vorticity concentrations are associated with the two recirculation bubbles in the wake. Furthermore, one positive $\bar{\omega}^*_y$ concentration with $\bar{\omega}^*_{y,max} = 3.6$ occurs at the lower edge of the rear window, which is ascribed to the corner vortex. Hereinafter, subscripts '*max*' and '*min*' denote the maximum vorticity concentrations of positive and negative signs, respectively.

Figure 5(*c*,*d*) presents time-averaged streamlines and the $\bar{\omega}^*_x$ contours in the (y, z) planes of $x^* = -0.09$ (above the rear window). The flow exhibits several features. First, a downwash flow occurs above $z^* \approx 0.76$, which is linked to flow separation from the roof. Second, an upwash flow takes place at z^* from 0.61 to 0.76, which is associated with the upstream and upward motion of flow from the base to the rear window within the upper recirculation bubble, as is evident from the streamlines in the (x, z) plane of $y^* = 0$ (figure 5*a*). Third, a flow moves toward the slanted surface below $z^* \approx 0.61$, which is connected to the reattachment of the flow separated from the upper edge of the base. As shown in the $\bar{\omega}^*_x$ contours (figure 5*d*), two concentrations marked by '*C*', the signatures of the well-known C-pillar vortices, occur behind the two side edges of the rear window, whose maximum magnitude reaches approximately 2.1 at (y^*, z^*) $\approx$ ($\pm$0.53, 0.83), resulting from a swirling motion. This motion is the rollup of shear layer coming off the sidewall about the side edge of the slanted surface, due to a pressure difference between flow at the sidewall and that over the rear window (Ahmed *et al.* 1984). The C-pillar

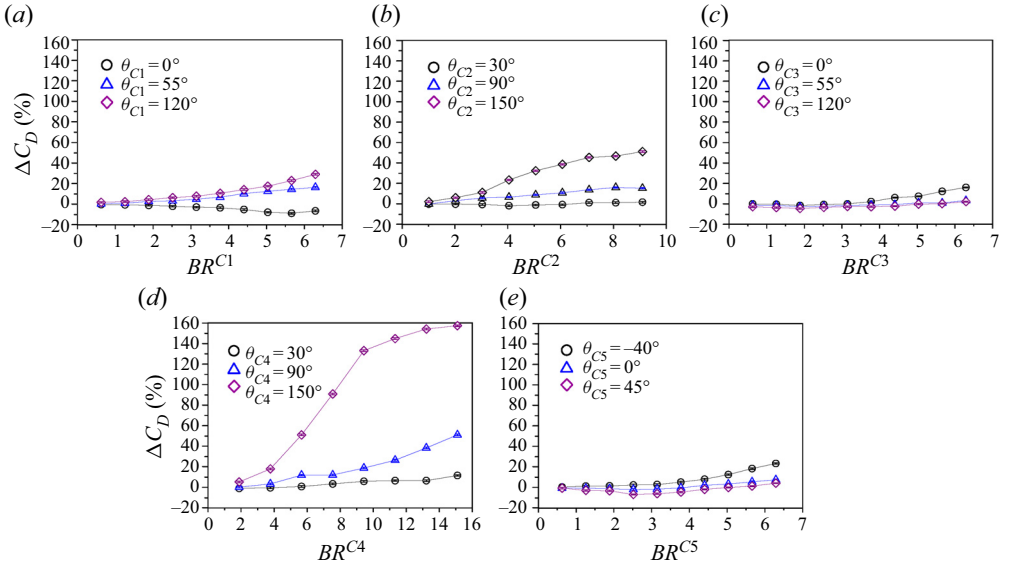

Figure 6. Dependence of the change ΔC_D in the drag coefficient on (*a*) blowing ratios BR^{C1}, (*b*) BR^{C2}, (*c*) BR^{C3}, (*d*) BR^{C4} and (*e*) BR^{C5} under individual C_1, C_2, C_3, C_4 and C_5 at various blowing angles ($Re = 1.7 \times 10^5$). The uncertainty bars of ΔC_D are calculated from $|\Delta C_D - \overline{\Delta C_D}|$.

vortices are much weaker in strength than their counterparts in the high-drag regime (e.g. Hucho & Sovran 1993); the maximum $\bar{\omega}_x^*$ of the former is ten times larger than that of the latter based on the PIV data measured in the (y, z) plane of $x^* = 0.2$ (Wang *et al.* 2013). A number of alternately signed $\bar{\omega}_x^*$ concentrations occur near the rear window. The C-pillar vortex may induce an inboard neighbouring vorticity concentration or a secondary vortex with an opposite sign (Zhang *et al.* 2015). For the same reason, this secondary vortex may induce another $\bar{\omega}_x^*$ concentration next to it.

4.2. *Combined actuations*

4.2.1. *Optimization of control parameters based on ACA algorithm*

The control performance under individual C_1, C_2, C_3, C_4 and C_5 is first investigated. Figure 6 shows the dependence of ΔC_D on the blowing ratio for the five individual actuations operated at different blowing angles. The uncertainty of ΔC_D is estimated to be within 1 %. It can be seen that the blowing angle produces a significant effect on the *DR* performance. Firstly, the drag can be either substantially decreased or increased by C_1, depending on θ_{C1} (figure 6*a*). At $\theta_{C1} = 0°$, the drag drops with increasing blowing ratio, the maximum *DR* being approximately 9 % when BR^{C1} reaches 5.7. Beyond this BR^{C1}, the drag grows. On the other hand, the drag rises with increasing BR^{C1} at $\theta_{C1} = 55°$ and 120°, ΔC_D reaching 17 % and 29 % at $BR^{C1} = 6.3$, respectively. Secondly, when C_2 is operated at $\theta_{C2} = 30°$, BR^{C2} produces little influence on the drag (figure 6*b*). This is not the case at $\theta_{C2} = 90°$and 150° where the drag increases by 16 % and 51 % at $BR^{C2} = 9.1$, respectively. Thirdly, there appears one critical blowing ratio $BR_{cr}^{C3} = 1.9$ under C_3 (figure 6*c*), regardless of θ_{C3}; the drag drops initially, reaching its minimum at $BR^{C3} = BR_{cr}^{C3}$, and then rises with increasing BR^{C3}. The maximum DRs are 2 %, 3 % and 5 % for $\theta_{C3} = 0°$, 55°and 120°, respectively. Fourthly, like C_2, C_4 achieves little

Cases	BR^{Ci}	$\langle\overline{C_p}\rangle_r$	$\langle\overline{C_p}\rangle_b$	$\langle\overline{C_p}\rangle$	$\Delta\langle\overline{C_p}\rangle_r$	$\Delta\langle\overline{C_p}\rangle_b$	$\Delta\langle\overline{C_p}\rangle$	DR
Base flow	—	−0.34	−0.27	−0.24	—	—	—	—
C_1	$BR^{C1}=5.7$	−0.43	−0.16	−0.21	−27 %	43 %	13 %	9 %
C_2	$BR^{C2}=4.0$	−0.38	−0.24	−0.23	−9 %	14 %	2 %	1 %
C_3	$BR^{C3}=1.9$	−0.29	−0.27	−0.22	15 %	2 %	7 %	5 %
C_4	$BR^{C4}=1.9$	−0.34	−0.27	−0.23	0 %	2 %	1 %	1 %
C_5	$BR^{C5}=2.5$	−0.30	−0.24	−0.21	12 %	14 %	12 %	7 %

Table 4. Spatially averaged pressure coefficients $\langle\overline{C_p}\rangle_r$, $\langle\overline{C_p}\rangle_b$ and $\langle\overline{C_p}\rangle$, their variations, and the corresponding DR under C_1 ($\theta_{C1}=0°$), C_2 ($\theta_{C2}=30°$), C_3 ($\theta_{C3}=120°$), C_4 ($\theta_{C4}=30°$) and C_5 ($\theta_{C5}=45°$).

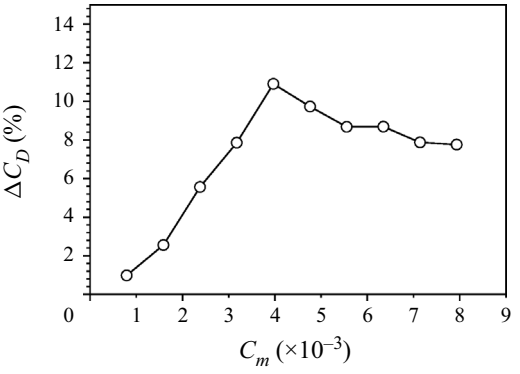

Figure 7. Dependence of DR on C_m under the combination of C_1, C_2, C_3, C_4 and C_5.

DR at $\theta_{C4}=30°$ (figure 6*d*). Finally, C_5 achieves its maximum DRs of 2 % and 7 % at $BR^{C5}=2.5$ for $\theta_{C5}=0°$ and 45°, respectively (figure 6*e*), but no DR for $\theta_{C5}=-45°$, irrespective of BR^{C5}. Table 4 shows $\langle\overline{C_p}\rangle_r$, $\langle\overline{C_p}\rangle_b$ and $\langle\overline{C_p}\rangle$ under each actuation, along with their variations and corresponding DR.

Individual C_1, C_2, C_3, C_4 and C_5 may have difficulty in controlling all or most of the predominant coherent structures, thus achieving rather limited DR. The DR under the combinations of C_1 ($\theta_{C1}=0°$), C_2 ($\theta_{C2}=30°$), C_3 ($\theta_{C3}=120°$), C_4 ($\theta_{C4}=30°$) and C_5 ($\theta_{C5}=45°$) is examined given the same blowing coefficient (C_m) for every actuation, which is defined by

$$C_m=\frac{Q}{U_\infty A}, \tag{4.2}$$

where Q is the volume flow rate (Fan *et al.* 2020*a*). The dependence of ΔC_D on C_m is presented in figure 7. The maximum DR reaches 11 % at $C_m=4.0\times10^{-3}$, slightly larger than that (9 %) achieved under individual actuations. One issue arises, that is, can we find a combination of these five actuations so that all the coherent structures can be effectively and simultaneously manipulated, producing a significantly more pronounced DR? In this section, we explore based on the AI control system introduced in § 3.1 the best strategy of the combined actuations for DR at $Re=1.7\times10^5$.

The ACA-based AI system searches for the optimal blowing ratios of all the five actuations. In the learning process, the cost of each ant was tested for 25 s, which is a compromise between the duration for time averaging and the converged cost function

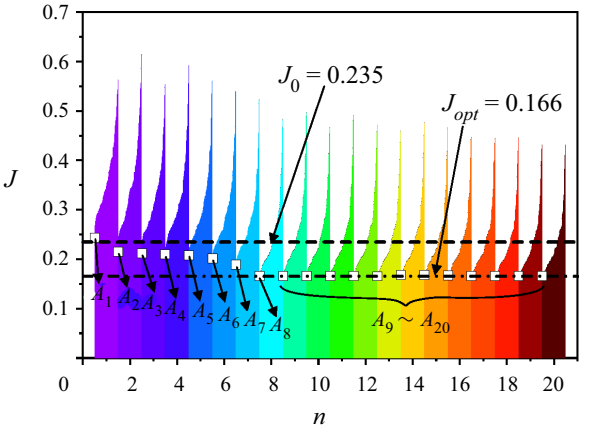

Figure 8. Learning curve of ACO control for the combined actuations of C_1 ($\theta_{C1} = 0°$), C_2 ($\theta_{C2} = 30°$), C_3 ($\theta_{C3} = 120°$), C_4 ($\theta_{C4} = 30°$) and C_5 ($\theta_{C5} = 45°$). Each colour bar consists of 100 values of J in a cycle. The square symbol highlights the smallest J or J_n of the best ant A_n in the *nth* cycle.

or cost. The learning curve of the AI control is presented in figure 8. Each cycle consists of 100 ants, corresponding to 100 costs, which form one colour bar. The square symbol highlights the best ant (A_n) of a cycle, corresponding to a minimum cost J_n, and the remaining costs of this cycle are arranged monotonously, following an ascending order. The trend shown by the square symbols reveals the evolution of the best ant from cycle $n = 1$ to 20, and the corresponding control parameters are shown in table 5. Here, A_1 is associated with $\boldsymbol{BR} = [6.0, 6.5, 4.3, 1.9, 1.8]^{\mathrm{T}}$, which produces a cost of $J_1 = 0.243$. This cost is 3 % higher than J_0 in the absence of forcing; $\Delta\langle\overline{C_p}\rangle$ associated with A_1 is approximately 2 %, corresponding to a *DR* of 1 %. This is not unexpected in view of (3.1) as β_p is relatively large, about 5 % of J_0. J_2 drops substantially by 8 % relatively to J_0, the corresponding $\Delta\langle\overline{C_p}\rangle$ and *DR* being 13 % and 8 %, respectively. In the third cycle, J_3 decreases further to 0.212, with a *DR* of 9 %. The control parameters of A_4, A_5 and A_6 are unchanged with $\boldsymbol{BR} = [6.1, 4.1, 4.6, 2.5, 1.6]^{\mathrm{T}}$. The maximum deviation in the cost between A_4, A_5 and A_6 is less than 1 %, within the measurement uncertainty, 2 %J_0, of J. A_7 corresponds to $\boldsymbol{BR} = [5.4, 3.7, 5.1, 2.1, 2.1]^{\mathrm{T}}$, yielding a drop in J by 20 % or a *DR* of 13 %. After that, J_8 drops substantially to 0.166 and remains unchanged for $n \geq 9$, implying a convergence of the cost that produces the highest ΔJ of −29 %, that is, the optimal or minimal cost J_{opt} is achieved. The optimized control law $\boldsymbol{B_{opt}}$ is $[5.8, 3.5, 4.9, 1.3, 1.8]^{\mathrm{T}}$, yielding an impressive *DR* of 18 %, significantly higher than any previously reported *DR* for a low-drag Ahmed body. The maximum *DR* obtained experimentally so far is only 4 % (Jahanmiri & Abbaspour 2011).

As shown in Zhou *et al.* (2020), a careful analysis of proximity maps may provide a good picture on the control laws identified and their distributions along with insight into the optimization process. Following Zhou *et al.* (2020) and Fan *et al.* (2020*a*), the considered ensemble of $\boldsymbol{BR_j}$ is represented as data points in the two-dimensional plane of the feature vectors $\boldsymbol{\gamma}_j = (\gamma_{j,1}, \gamma_{j,2})$, where $j = 1, 2, \ldots, N \times M$, so that the distance between the feature vectors is an indicator of the difference between the control laws. The r.m.s.-averaged

Cases	BR^{C1}	BR^{C2}	BR^{C3}	BR^{C4}	BR^{C5}	J	ΔJ	$\Delta\langle\overline{C_p}\rangle$	DR
A_1	6.0	6.5	4.3	1.9	1.8	0.243	3 %	2 %	1 %
A_2	4.8	6.6	4.0	3.5	2.9	0.215	−8 %	13 %	8 %
A_3	5.9	7.1	4.2	2.5	1.7	0.212	−10 %	16 %	9 %
A_4–A_6	6.1	4.1	4.6	2.5	1.6	0.202	−14 %	18 %	11 %
A_7	5.4	3.7	5.1	2.1	2.1	0.189	−20 %	23 %	13 %
A_8–A_{20}	5.8	3.5	4.9	1.3	1.8	0.166	−29 %	32 %	18 %

Table 5. Control parameters and performances of the best ants A_i ($i = 1, 2, \ldots, 20$), as marked by square symbols in figure 8.

Euclidean distance M_{jk} ($j, k = 1, 2, \ldots, N \times M$) between $\boldsymbol{BR_j}$ and $\boldsymbol{BR_k}$ is given by

$$M_{jk} = \sqrt{\sum_{i}^{5} \left(\frac{BR_j^{Ci} - BR_k^{Ci}}{BR_{mx}^{Ci}} \right)^2}, \tag{4.3}$$

where the subscript 'mx' denotes the maximal BR^{Ci} ($i = 1, 2, \ldots, 5$) in tests. Figure 9 presents the proximity map of the 1000 control laws found in the first 10 cycles in a two-dimensional plane, where the underlying metric between two control laws $\boldsymbol{BR_j}$ and $\boldsymbol{BR_k}$ is given by $\boldsymbol{D} = (D_{jk})$, *viz.*

$$D_{jk} = M_{jk} + \lambda |J_j - J_k|, \tag{4.4}$$

where λ is the penalty coefficient. The parameter λ is chosen so that the maximum actuation distance of M_{jk} is equal to the maximum difference in the performance terms. The classical multi-dimensional scaling (Cox & Cox 2001) is used to determine γ_1 and γ_2 for the matrix $\boldsymbol{D}$ so that the length of a feature vector or distance between different control laws can be preserved, yielding

$$\sum_{j=1}^{N\times M} \sum_{k=1}^{N\times M} (||\gamma_j - \gamma_k|| - D_{jk})^2 = min, \tag{4.5}$$

where *min* denotes the minimum value. Control landscape or proximity map is constructed from the three-dimensional data points $(\gamma_{j,1}, \gamma_{j,2}, J_j), j = 1, 2, \ldots, N \times M$. An unstructured grid from the Delaunay triangulation is used to connect the two-dimensional feature vectors (Kaiser *et al.* 2017). The J-values in each mesh triangle $j_1, j_2, j_3 \in \{1, \ldots, N \times M\}$ are interpolated from the known values at the vertices J_{j1}, J_{j2}, J_{j3}. For $n = 1$, the best ant occurs at $(\gamma_1, \gamma_2) = (0, -0.09)$. As n increases, A_n is seen to move toward its optimum, reaching A_8 at $(\gamma_1, \gamma_2) = (-0.24, 0.12)$. The searching path from A_1 to A_8 follows a rather straight line, indicating an effectiveness and efficiency of the ACA in searching the optimal control law. The AI control takes only 800 test runs to find the optimal combination of actuations.

The γ_1 and γ_2 have technically no *a priori* meaning. However, a careful analysis of the variation in $\boldsymbol{BR}$ with the optimal control performance may cast light upon the sensitivity of the control performance to individual actuations and associated input energies. Figure 10 shows the dependence of the upper and lower limits for BR^{Ci} ($i = 1, 2, 3, 4$ or 5), denoted by BR_{upp}^{Ci} and BR_{low}^{Ci}, respectively, on a small departure of J from its optimal value J_{opt}, say $J_{opt} + \delta$, $J_{opt} + 2\delta$ and $J_{opt} + 3\delta$, where $\delta = 0.01 J_{opt}$. This dependence may indicate

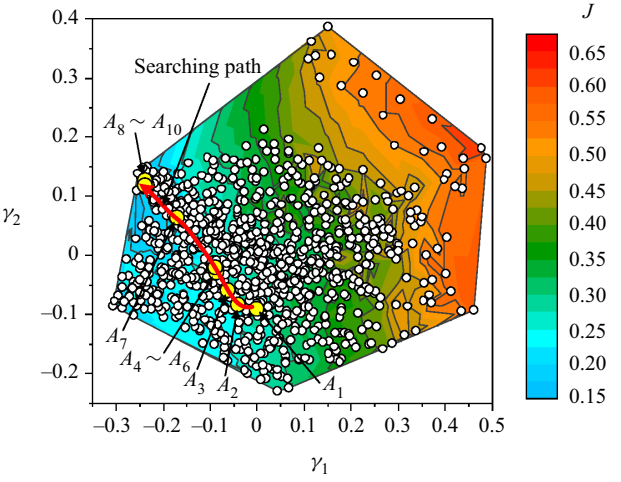

Figure 9. Control landscape produced from the 1000 control laws, each corresponding to a white circle, obtained in the first 10 cycles of the learning process. The yellow circle denotes the best control law of each cycle.

whether the lowest J or optimal control is sensitive to BR^{Ci}. Then, the maximal interval of BR^{Ci} is given by

$$\Delta BR^{Ci} = BR^{Ci}_{upp} - BR^{Ci}_{low}. \tag{4.6}$$

A small change in BR^{C1} from 5.9 to 5.0 may lead to a deteriorated J from J_{opt} to $J_{opt} + \delta$. The range grows substantially to BR^{C1} from 4.0 to 6.0 as J is relaxed from J_{opt} to $J_{opt} + 2\delta$. When J is further relaxed to $J_{opt} - (J_{opt} + 3\delta)$, the BR^{C1} range grows to 2.8–6.0. A similar trend of the blowing ratio range is also observed for BR^{Ci} ($i = 2$, 3, 4 or 5). The observation suggests that a small sacrifice in J may lead to a substantial reduction in BR^{Ci} or saving in the input energy. The ΔBR^{C1} is approximately 0.9 from J_{opt} to $J_{opt} + \delta$, which is comparable to ΔBR^{C5} (1.0) but is appreciably smaller than ΔBR^{C2} (1.5), ΔBR^{C3} (2.2) or ΔBR^{C4} (1.4). The ΔBR^{C3} is the largest, exceeding $2\Delta BR^{C1}$ or $2\Delta BR^{C5}$. The results indicate that the DR, when approaching its maximum, is less sensitive to BR^{C3} than the other four blowing ratios. A relaxation in J from J_{opt} to $J_{opt} + 2\delta$ leads to a moderate increase in ΔBR^{Ci} ($i = 1, 2, \ldots, 5$) from 0.9, 1.5, 2.2, 1.4 and 1.0 to 2.0, 3.2, 3.5, 2.8 and 2.0, respectively. When this relaxation is further raised to $J_{opt} + 3\delta$, ΔBR^{C1} and ΔBR^{C5} rise to 3.2 and 2.8, respectively; however, ΔBR^{C2}, ΔBR^{C3} and ΔBR^{C4} grow more significantly to 6.4, 4.3 and 4.2, respectively, ΔBR^{C2} being the largest. The observation implies that the near-optimal control is quite sensitive to BR^{C1} and BR^{C5}, but less so to BR^{C2}, BR^{C3} or BR^{C4}. It seems plausible that one way to enhance the control efficiency is to reduce to a certain extent the power input of control while maintaining a near-maximum DR. Evidently, being sensitive to the maximum DR, BR^{C1} and BR^{C5} should be kept near their optimal values in order to maximize the DR. On the other hand, we may reduce BR^{C2}, BR^{C3} or BR^{C4}, without sacrificing much the DR, for the purpose of a rather substantial saving in the power input.

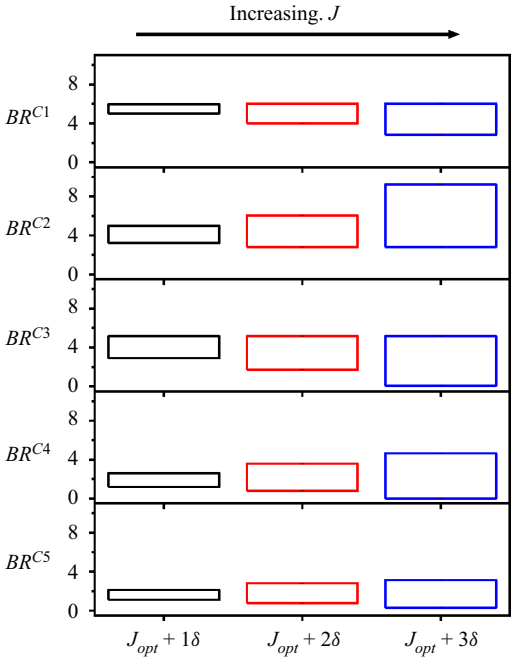

Figure 10. Dependence of the upper and lower limits for BR^{Ci} ($i=1$, 2, 3, 4 or 5) on a small departure of J from its optimal value J_{opt}, i.e. $J_{opt}+\delta$, $J_{opt}+2\delta$ and $J_{opt}+3\delta$, where $\delta=0.01J_{opt}$.

4.2.2. *Control efficiency*

The active control requires energy input to produce DR. Therefore, it is important to determine the ratio of the power saved from the DR to the control input power P_{Ci} ($i=1$, 2, … 5) which is an important indicator to evaluate the efficiency of the control (Choi, Jeon & Kim 2008). The control efficiency η is defined by

$$\eta = \frac{\Delta F_D U_\infty}{\sum_{i=1}^{5} P_{Ci}}, \tag{4.7}$$

where ΔF_D denotes the decrease in drag under control (e.g. Choi *et al.* 2008; Zhang *et al.* 2018) and P_{Ci} may be calculated from (3.3). From (4.7), the power saved from reduced drag exceeds the control input power if η exceeds unity.

Figure 11 presents the dependence of η on individual blowing ratios for C_1 ($\theta_{C1}=0°$), C_2 ($\theta_{C2}=30°$), C_3 ($\theta_{C3}=120°$), C_4 ($\theta_{C4}=30°$) and C_5 ($\theta_{C5}=45°$). For all actuations, the maximum η occurs at small BR and then declines continuously with increased BR. At $BR\approx 0.6$, η reaches approximately 2.6, 31.8 and 4.5 under C_1, C_3 and C_5, respectively. Nevertheless, η becomes smaller than unity when BR^{C1}, BR^{C2} and BR^{C3} exceed 1.3, 2.5 and 3.1, respectively, that is, the power saved from reduced drag is less than the control input power. On the other hand, the maximum η is only 0.2 and 0.6 for C_2 and C_4, respectively, indicating inefficient controls.

To gain an overall picture on how DR and η vary with increasing n and how they could be connected to each other, let us examine the proximity maps (figure 12) of control laws

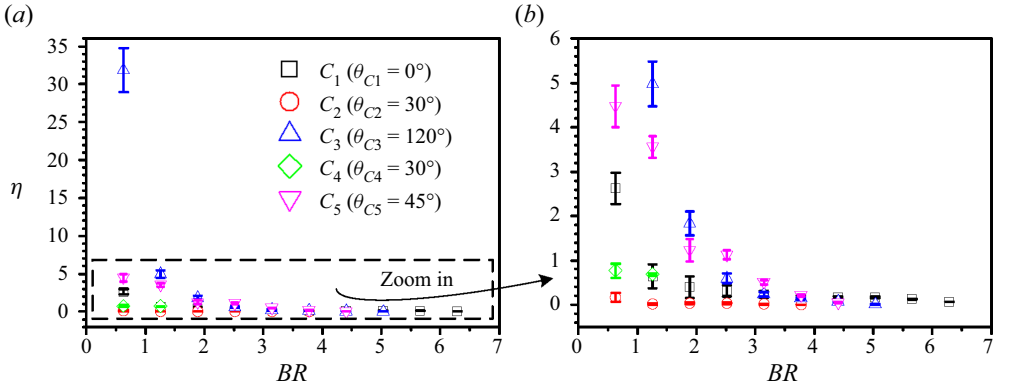

Figure 11. (*a*) Dependence of the control efficiency η on BR under individual C_1, C_2, C_3, C_4 and C_5. (*b*) Zoom in plot for $0 < \eta < 6$. The uncertainty bars of η are calculated by $|\Delta F_D - \overline{\Delta F_D}|\, U_\infty / \sum_{i=1}^{5} P_{Ci}$.

for cycles 1, 7, 12 and 15 along with the normalized control power input, *viz.*

$$P_c^* = \frac{\sum_{i=1}^{5} P_{Ci}}{U_\infty F_D}. \tag{4.8}$$

Note that the J-contours in the figure are generated from 2000 control laws in 20 cycles. The diameter of white circles in the figure indicates the magnitude of P_c^*. There appears a correlation between the level of J and γ_1; the former displays in general a growth with the latter increasing. However, γ_2 correlates with neither J nor P_c^*. The control laws occur largely in the right half of the phase plane in the first cycle; they shift gradually toward the left or the negative γ_1 direction and take place within a narrower range of γ_1 with increasing n. The learning process is converged at $n = 8$ in terms of J when the maximum DR (18 %) is obtained. This maximum is, however, associated with a very small η, only 0.13. However, with n increasing further, both DR and the corresponding η continue to evolve in spite of a negligible change in J. Define E_n ($n = 1, 2, \ldots, 20$) as the control law with the highest η in the nth cycle; E_7 corresponds to $\boldsymbol{BR} = [0.7, 0.4, 0.5, 0.7, 0.6]^{\mathrm{T}}$ with $P_c^* = 0.004$, producing a large η of 25.7 and a DR of 10 %. As the present cost contains the control power input (3.1), there is an overall decline in P_c^* with increasing n; for example, the largest P_c^* drops from 11.9 in $n = 12$ to 6.7 in $n = 15$. Accordingly, η is 1.1 for E_{12} ($\boldsymbol{BR} = [2.6, 2.6, 0.2, 0.2, 0.3]^{\mathrm{T}}$) and 5.8 for E_{15} ($\boldsymbol{BR} = [1.9, 0.3, 0.2, 0.5, 0.5]^{\mathrm{T}}$), their corresponding DR being 16 % and 15 %, respectively. The latter requires less than 20 % of input energy consumed by the former with a sacrifice in DR by only 1 %. One may surmise that the physical mechanisms must differ between the cases of a pronounced DR but a small η and a less pronounced DR but a substantially increased η, which will be discussed in the next two subsections.

Jahanmiri & Abbaspour (2011) attained a DR of only 4 % with a relatively large η of 62.1, who deployed a combination of steady suction near the upper edge of rear window and steady blowing at the mid-height of the base of a low-drag Ahmed body with $\varphi = 45°$. Edwige *et al.* (2018) obtained a DR of 2 % with a η of 7.6, who applied pulsed blowing along the two side edges of the base of an Ahmed body ($\varphi = 47°$). Evidently, the combination of C_1, C_2, C_3, C_4 and C_5 found by the AI control achieves a much

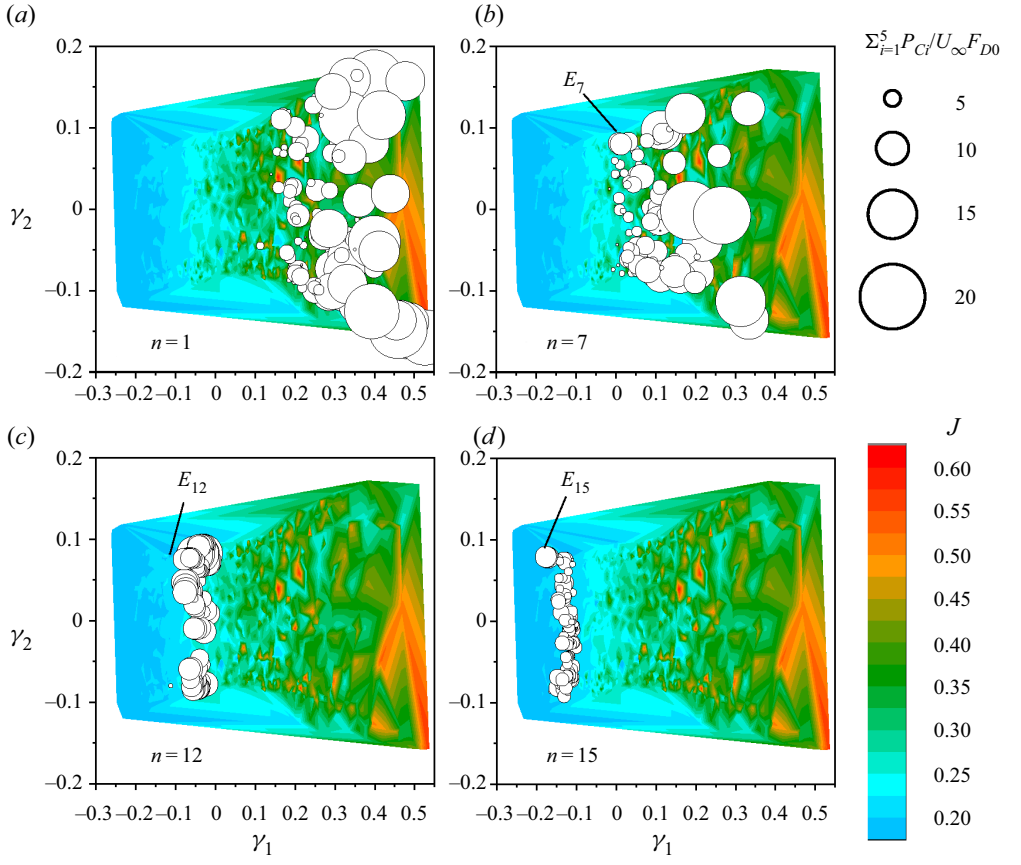

Figure 12. Control landscape associated with cycles 1, 7, 12 and 15 (100 ants for each cycle). The contours of J are produced from 2000 control laws in 20 cycles. Each circle represents a control law, whose diameter is proportional to the power input $\sum_{i=1}^{5} P_{Ci}/U_\infty F_{D0}$.

better performance in terms of both control efficiency and *DR* and may provide a valuable guidance for the design of effective and efficient *DR* schemes for engineering applications.

4.2.3. *Flow structure under the optimal control*

Consider the optimal control when the largest *DR* is achieved under the optimized combination of actuations (A_8–A_{20}). Figure 13 presents the distribution of $\overline{C_p}$ on the rear window and the base with and without control. The uncertainty of $\overline{C_p}$ is estimated to be 0.005, approximately 2 % of $\langle \overline{C_{p0}} \rangle$ (-0.24). The $\overline{C_p}$ distribution of the base flow displays a pressure minimum near the lower edge of the rear window and at the upper edge of the base (figure 13*a*), which is ascribed to the occurrence of a corner vortex (Liu *et al.* 2021). In the symmetry plane, $\overline{C_p}$ declines from -0.34 to -0.36 with decreasing z^* from 0.54 to 0.78 over the rear window, and from -0.21 to -0.34 with increasing z^* over $z^* = 0.12$–0.39. Under the optimal control (figure 13*b*), a significant high-pressure region arises near the lower edge centre of the rear window, where $\overline{C_p}$ rises by 287 %. As will be seen later, this marked pressure rise is associated with the stagnated flow above the lower end of the slanted surface about the symmetry plane. Furthermore, $\overline{C_p}$ near the middle of the side edge of the rear window goes up by approximately 50 %. However, the pressure near the

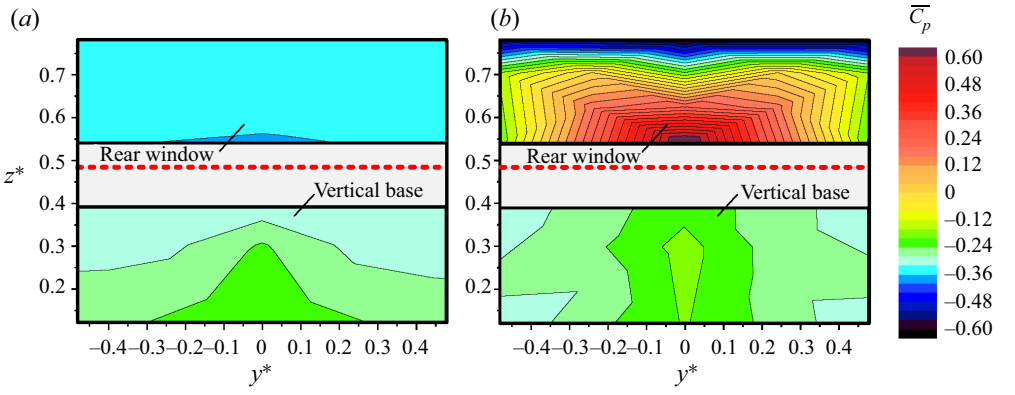

Figure 13. Distributions of $\overline{C_p}$ on the rear window and base of the Ahmed body: (*a*) the unforced flow, (*b*) under the optimized combination of actuations. The red-coloured dotted line denotes the upper edge of the vertical base.

upper edge of the rear window dips substantially, with $\Delta\overline{C_p}$ being −87 % in the middle region. The combined effect is an increase in $\langle\overline{C_p}\rangle_r$ by 72 %. On the vertical base, $\overline{C_p}$ in the symmetry plane rises by 30 %, 22 % and 7 % at $z^* = 0.39$, 0.3 and 0.12, respectively. At the lateral side of the base, the pressure near the mid-height of the base grows slightly by 5 %, but drops by 19 % near the lower edge of the base. Overall, $\langle\overline{C_p}\rangle_b$ increases by 4 % as compared with the unforced flow.

Since the flow is highly three-dimensional, we examine the PIV data measured in three orthogonal planes of the wake under the optimal control in order to understand the flow physics and *DR* mechanisms. Figure 14 presents the time-averaged streamlines and the contours of velocity magnitude $\overline{U_{xz}}^*$ in the (x, z) plane. Here, C_1 yields a relatively small separation bubble over the rear window (figure 14), which is distinct from the unforced flow characterized by a full separation over the rear window (figure 5*a*). This separation bubble creates a small low-pressure region near the upper edge of the rear window (figure 13*b*). One saddle point, marked by 'S_{C1}', occurs very close to the lower end of the rear window, implying stagnated flow there, where the flow velocity is zero (e.g. Zhou & Antonia 1994). This stagnated flow may be responsible for the impressive increase, almost three times, in $\overline{C_p}$ near the mid lower edge of the slanted surface. The streamlines (figure 14*a*) indicate that the attaching flow along the rear window interacts with the upward and upstream blowing of C_3, resulting in the stagnated flow near (x^*, z^*) = (−0.04, 0.53). Also, C_3 acts to force the flow, separated from the upper edge of the base, to deflect upward, resulting in the elongation of the two recirculation bubbles behind the base. The values of l_u^* and l_l^* reach 0.77 and 0.59, respectively, exceeding substantially their counterparts (0.31 and 0.29) under C_1. The elongated bubbles account for a downstream shift in their centres, which is accompanied by an increase in the base pressure. Behind the two bubbles, another saddle point (S_{C2}) occurs at (x^*, z^*) = (0.62, 0.02), which is a result of interaction between the two bubbles (Zhang *et al.* 2015). Meanwhile, the alternate emanation of coherent structures is eliminated, as supported by the disappearance of the peak at $f^* = 0.3$ in E_u (not shown). In the off-symmetry plane of $y^* = 0.36$ (figure 14*b*), however, the two bubbles contract longitudinally, taking their centres, as well as the saddle point (S_{L2}), close to the base, compared with those in the symmetry plane. This is an indication that the legs of the two bubbles are tilted upstream. The 'legs' refer to the vortical structures near the two lateral sides of the bubble

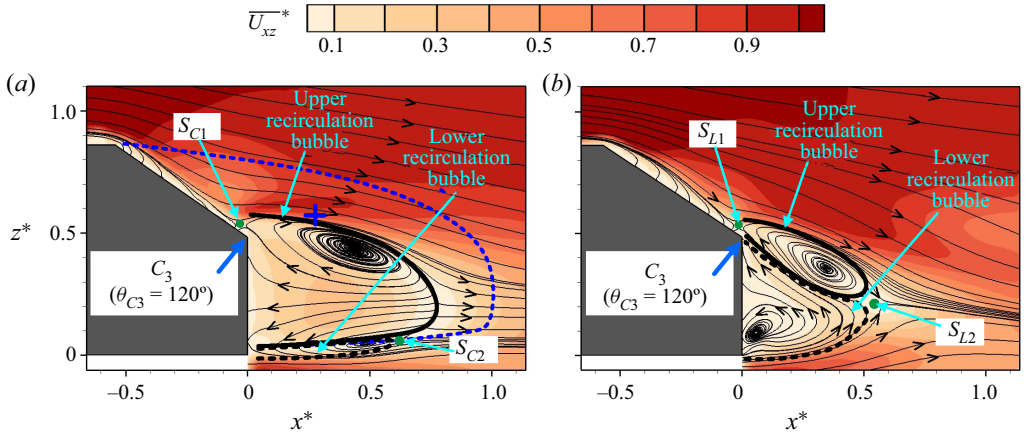

Figure 14. Time-averaged streamlines superimposed with the $\overline{U_{xz}}^*$ contours in the (x, z) planes of (*a*) $y^* = 0$ and (*b*) $y^* = 0.36$ under the optimized combination of actuations, where the green dots denote the saddle points. In (*a*), the blue symbols '+' denote the focus and the blue broken lines indicate the bubble size in the unforced flow determined from the streamlines in figure 5(*a*).

(Liu *et al.* 2021). The other saddle point (S_{L1}) near the lower edge of the rear window is also discernible in the plane of $y^* = 0.36$, which accounts for a rise in pressure by 123 % near the lower edge of the window in this plane (figure 13*b*).

The longitudinal structures may be well visualized from the time-averaged streamlines and the contours of velocity magnitude $\overline{U_{yz}}^*$ and $\bar{\omega}_x^*$ in the (y, z) planes of $x^* = -0.09$ and 0.43. The C-pillar vortices appear enhanced appreciably in both size and strength (figure 15*a*), compared with the unforced flow (figure 5*d*). However, their strength in terms of $\bar{\omega}_{x,max}^*$ is very small, only 2.9, at $x^* = -0.09$, compared with that (20.6) under C_1. This is due to an overall increase in the surface pressure on the rear window, and the decreased pressure difference between the flow over the window and that coming off the sidewall of the body weakens the C-pillar vortex. Meanwhile, the blowing near the lower edge of the rear window generates outboard one negatively signed vortical structure (figure 15*a*), as denoted by '*E*'. This structure takes place below the C-pillar vortex and close to the slanted surface, with its centre, identified with $\bar{\omega}_{x,min}^*$, at $(y^*, z^*) \approx (0.41, 0.57)$. Consequently, $\overline{C_p}$ near the lower end of the side edge of rear window is 44 % higher than the unforced flow (figure 13). The streamlines in the plane of $x^* = 0.43$ behind the base (figure 15*b*) show two foci at $(y^*, z^*) = (-0.23, 0.40)$ and $(-0.20, 0.08)$, which are connected to the legs of the upper and lower recirculation bubbles, respectively. The rotation directions of the streamlines around the upper and lower foci are anti-clockwise and clockwise, respectively, conforming to the upstream tilting legs of the two bubbles, as evidenced in the PIV-measured streamlines in the (x, z) planes of $y^* = 0$ and 0.36 (figure 14). As shown in the $\bar{\omega}_x^*$ contours in the plane of $x^* = 0.43$, the legs of the upper and lower bubbles are characterized by the negative- and positive-signed vorticity concentrations, respectively. On the other hand, the trailing legs of the upper recirculation bubble tilt downstream in the base flow (Liu *et al.* 2021). The change in the two bubbles may be largely responsible for the decrease by 19 % in $\overline{C_p}$ near the bottom of side edge of the base.

It is also insightful to examine the flow structure in the (x, y) plane. The streamlines in the plane of $z^* = 0.67$ of the unforced flow display a reverse flow at $-0.27 < x^* < 0$ above the rear window (figure 16*a*), which is linked to the upstream motion from the vertical base to the rear window within the upper recirculation bubble (figure 5*a*).

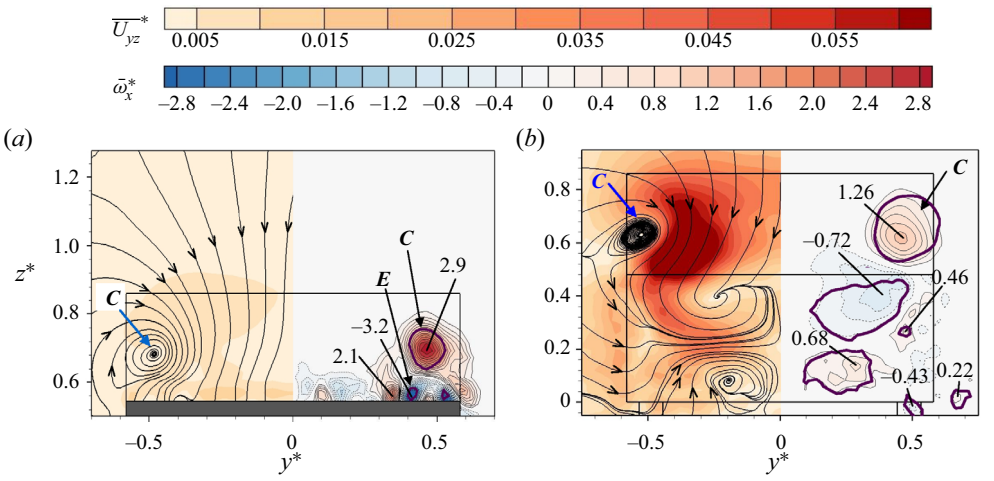

Figure 15. Time-averaged streamlines, superimposed with the $\overline{U_{yz}}^*$ contours, and $\bar{\omega}_x^*$-contours in the (y, z) planes of (*a*) $x^* = -0.09$ and (*b*) 0.43 under the optimized combination of actuations, where the thick purple closed contours correspond to the time-averaged swirling strength $\overline{\lambda_{ci}^2}^* = 0.001$.

For $x^* > 0$, the flow moves downstream. The $\bar{\omega}_z^*$ contours show a strip of positively signed vorticity concentration near the side edge of the rear window (figure 16*a*), which appears deflected toward the symmetry plane at $x^* \approx 0$. This $\bar{\omega}_z^*$ concentration is ascribed to the side vortices wrapped around the C-pillar vortex (Liu *et al.* 2021). In the (x, z) plane of $z^* = 0.24$, the flow separates from the side edge of the base and rolls up, forming one recirculation bubble behind the vertical base whose centre occurs at $(x^*, y^*) = (0.45, 0.42)$ (figure 16*b*), as confirmed by the positive $\bar{\omega}_z^*$ concentration behind the lateral side of the base. This structure may be associated with the lower recirculation bubble as supported by the streamlines in the (x, z) plane of $y^* = 0.36$, where this bubble spans $z^* = 0$–0.35 at $x^* = 0.56$. When the optimized combination of actuations is applied, the reverse flow in the plane of $z^* = 0.67$ above the rear window disappears (figure 16*c*), due to the diminished flow separation over slanted surface (figure 14). Furthermore, the $\bar{\omega}_z^*$ concentration near the lateral side of the rear window contracts longitudinally, though its inward tilting is strengthened. This is not unexpected since the C-pillar vortex is significantly enhanced in strength by control. The recirculation bubble behind the base shrinks longitudinally (figure 16*d*), cf. figure 16(*b*). The shear layer separated from the side edge of the base is inward deflected (figure 16*d*). The separation angle β between the streamwise direction and the local tangential velocity of the streamline through the flow separation point rises from 7.5° to 24.5° with increasing x^* from 0 to 0.5 under control, substantially larger than those (from 3.5° to 9.7°) in unforced flow. The ensuing boat tailing effect contributes to an increase in the surface pressure on the base. The combined effects lead to an increase in $\langle \overline{C_p} \rangle_b$ by 4 %.

A conceptual model is proposed in figure 17 for the altered flow structure and hence the *DR* mechanism under the optimized combination of actuations. There are a number of significant changes in the flow structure over the window compared with the unforced flow (Liu *et al.* 2021). The pair of C-pillar vortices grow markedly in strength, inducing a downwash flow between them and resulting in flow reattachment over the rear window, albeit with one small separation bubble near the upper edge of the rear window (figures 14 and 15). However, the C-pillar vortices remain greatly weaker than their counterpart in

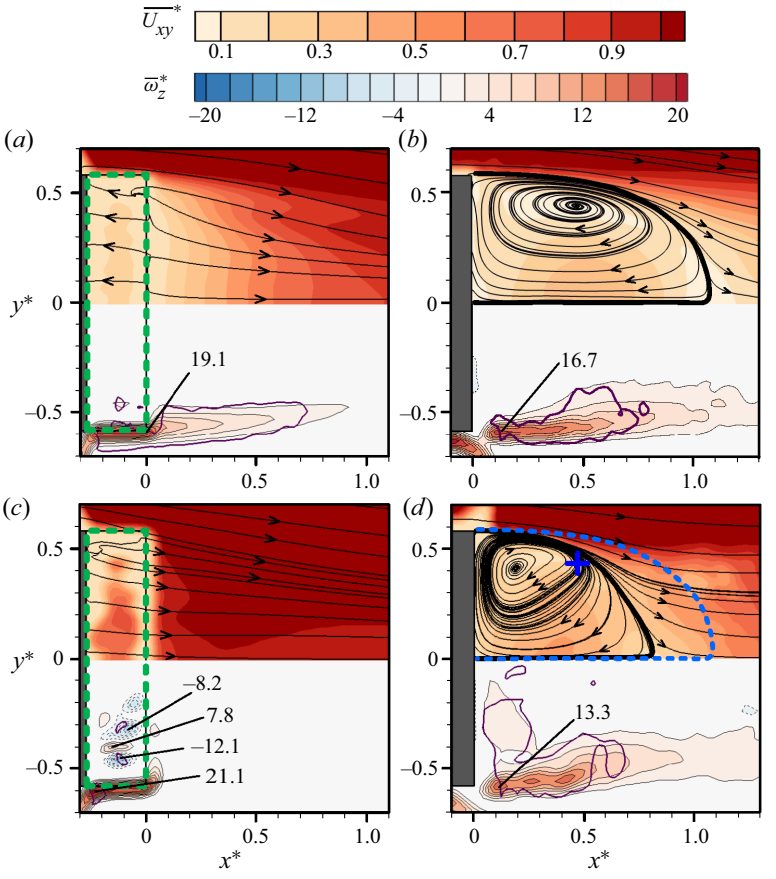

Figure 16. Time-averaged streamlines, superimposed with the $\overline{U_{xy}}^*$-contours, and $\bar{\omega}_z^*$-contours in the (x, y) planes: (a, c) $z^* = 0.67$, (b, d) 0.24. The local maximum vorticity levels $\bar{\omega}_{z,max}^*$ and $\bar{\omega}_{z,min}^*$ are marked. The thick purple closed contours correspond to the time-averaged swirling strength $\overline{\lambda_{ci}^2}^* = 0.1$. ($a$, b) Unforced flow, (c, d) under the optimized combination of actuations. The green-coloured rectangle in (a, c) denotes the region of the rear window projected to the plane of $z^* = 0.67$. In (d), the blue symbol '+' denotes the focus and the blue broken lines indicate the bubble size in the unforced flow determined from the streamlines in (b).

the high-drag regime (Zhang *et al.* 2018), implying a small rise in the energy loss due to the formation of the vortices. The reattached flow, interacting with the blowing of C_3, generates a patch of stagnated flow near the lower edge of the window. As a result, $\overline{C_p}$ near the mid lower edge of the rear window is raised by 287 % (figure 13), accounting for a rise in $\langle \overline{C_p} \rangle_r$ by 72 %. Furthermore, a boat tailing effect is created by the inward deflection of separated shear layers from the side edges of base (figure 16), causing a rise in $\langle \overline{C_p} \rangle_b$ by 4 %. The present *DR* mechanism is distinct from those previously reported. Zhang *et al.* (2018) cut down the drag by 29 % for a high-drag Ahmed body because the flow is changed to the low-drag regime. In case of the square-back Ahmed body, the *DR* mechanism is either ascribed to the suppressed wake bi-stability (e.g. Brackston *et al.* 2016; Li *et al.* 2016; Evstafyeva, Morgans & Dalla Longa 2017) or attributed to the modified shape of the mean recirculation region behind the base such as the boat tailing effect (e.g. Barros *et al.* 2016; Fan *et al.* 2020*a*; Haffner *et al.* 2020) and an elongation of the recirculation region (e.g. Barros *et al.* 2014; Lorite-Díez *et al.* 2020*b*).

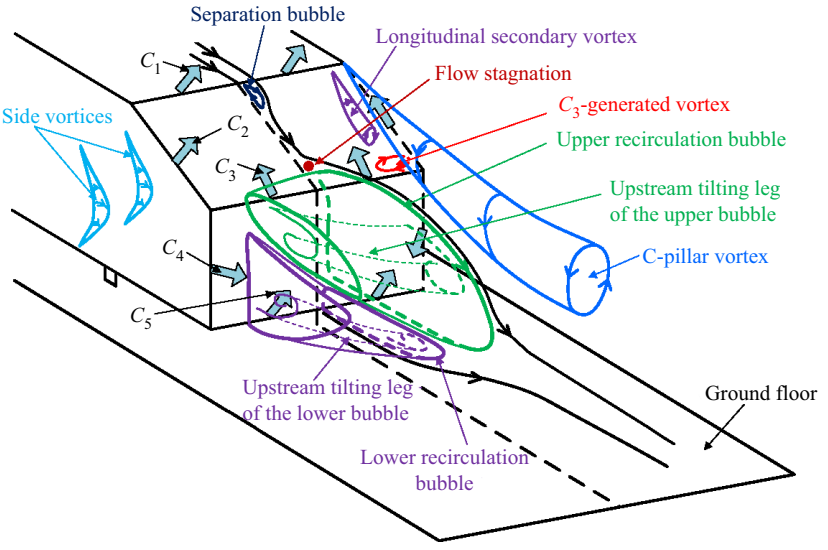

Figure 17. Conceptual model of flow structure under the optimized combination of actuations.

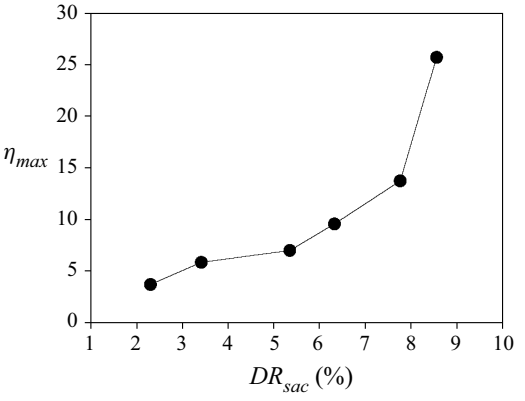

Figure 18. Dependence of η_{max} on DR_{sac} at intervals $[i\,\%, i+1\,\%]$ $(i = 1, 2, 3, \ldots, 8)$ from 38 control laws with $\eta > 1$.

4.2.4. *Flow structure associated with an efficient control*

It has been found from a close examination of all the 2000 control laws that 38 individuals produce an efficient control, i.e. $\eta > 1$, with $\eta = 1.1$–25.7 and corresponding DR is 10 %–16 %. Let us consider sacrificing some DR for a higher efficiency and denote this sacrificed amount from the maximum (18 %) as DR_{sac} and then $DR_{sac} = 2\,\%$–$8\,\%$. Figure 18 presents the variation in the maximum efficiency η_{max} for each increment ($i\,\%$, $i+1\,\%$, $i = 1, 2, \ldots, 8$) in DR_{sac}, and the corresponding control laws can be found in table 6. The η_{max} displays a continuous growth with increasing DR_{sac}. The η_{max} rises moderately from 3.7 to 7.0 given a small DR_{sac} from 2 % to 5 % but then rapidly from 9.6 to 25.7 from $DR_{sac} = 6\,\%$ to 8 %. The increase in η_{max} with DR_{sac} is mainly connected to the decreasing BR^{C1}, which drops from 2.1 to 0.7 from $\eta_{max} = 3.7$ to 25.7 (table 6).

It is important to understand why an efficient control can be achieved. As such, we take a close look at the flow around the body under the control law $\boldsymbol{BR_e}$ that achieves

Cases	BR^{C1}	BR^{C2}	BR^{C3}	BR^{C4}	BR^{C5}	DR	DR_{sac}	η
Combination #1	2.1	0.3	0.5	0.3	1.3	16 %	2 %	3.7
Combination #2	1.4	1.1	1.1	0.5	1.0	15 %	3 %	5.8
Combination #3	1.0	0.3	0.1	1.5	1.2	13 %	5 %	7.0
Combination #4	0.4	0.2	0.2	0.3	1.5	12 %	6 %	9.6
Combination #5	0.8	1.1	0.3	0.2	0.3	11 %	7 %	13.7
Combination #6	0.7	0.4	0.5	0.7	0.6	10 %	8 %	25.7

Table 6. Control parameters and performances for different combinations of C_1 ($\theta_{C1} = 0°$), C_2 ($\theta_{C2} = 30°$), C_3 ($\theta_{C3} = 120°$), C_4 ($\theta_{C4} = 30°$) and C_5 ($\theta_{C5} = 45°$), $Re = 1.7 \times 10^5$.

the highest η of 25.7. There is an overall increase in pressure on the rear window and base of the body under control, as is evident when comparing the $\overline{C_p}$ distribution without control (figure 13*a*) with that under the control law $\boldsymbol{BR_e}$ that achieves the highest η of 25.7 (figure 19), $\langle\overline{C_p}\rangle_r$ and $\langle\overline{C_p}\rangle_b$ rising by 12 % and 9 %, respectively. As a result, $\langle\overline{C_p}\rangle$ goes up by 11 % under control. Note that the pressure distribution under $\boldsymbol{BR_e}$ is quite different from that under the optimal control. The low-pressure and very-high-pressure regions near the upper and mid lower edges, respectively, of the window (figure 13*b*) cannot be seen under $\boldsymbol{BR_e}$ (figure 19). This is reasonable as the flow structure between the two cases exhibits several distinct differences. Firstly, the pressure recovery on the rear window near the symmetry plane under $\boldsymbol{BR_e}$, where $\overline{C_p}$ goes up by 14 %, 12 % and 11 % at $z^* = 0.78$, 0.62 and 0.54, respectively, is connected to a downstream shift in the centre of the upper recirculation bubble (Zhang *et al.* 2018), as shown in figure 20(*a*) (cf. figure 5*a*). A relatively small BR^{C1} (=0.7) fails to eradicate flow separation from the upper edge of the window. Under the optimal control, on the other hand, the pressure recovery on the window is mainly ascribed to the stagnated flow near the mid lower edge of the window, resulting in a much higher rise (287 %) in $\overline{C_p}$ (figure 13*b*). Secondly, one strip of positive $\bar{\omega}_y^*$ concentration takes place in the lower part of the window and the upper part of the base under $\boldsymbol{BR_e}$ (figure 20*b*), where $\bar{\omega}_{y,max}^*$ reaches 8.1, apparently due to the presence of the corner vortex. However, the corner vortex is absent under the optimal control. This is not unexpected in view of the much lower BR^{C3} (=0.5) under $\boldsymbol{BR_e}$ than that (4.9) under the optimal control. Thirdly, under $\boldsymbol{BR_e}$, the lower recirculation bubble covers most part of the base (figure 20*a*), extending significantly both vertically and longitudinally, which accounts for a rise in $\overline{C_p}$ on the base ($y^* = 0$) by 7 % – 9 % (figure 19). In contrast, it is the upper recirculation bubble that covers almost the entire base under the optimal control (figure 14*a*), and the high-pressure stagnated flow near the lower edge of the window contributes to a pressure recovery near the upper edge of the base, which is supported by a significant rise in $\overline{C_p}$ near the mid upper edge of base by 30 % (figure 13*b*).

The C-pillar vortex remains discernible under $\boldsymbol{BR_e}$, as suggested by the $\bar{\omega}_x^*$-contours in the (y, z) plane of $x^* = 0.43$ (figure 21*a*) where a vorticity concentration, superimposed by the contour of $\overline{\lambda_{ci}^2}^* = 0.001$, is evident near ($y^*$, z^*) = (0.48, 0.78). It is worth mentioning that, in the (y, z) plane of $x^* = -0.09$ above the rear window, $\bar{\omega}_{x,max}^*$ associated with the C-pillar vortex is 1.4 (not shown), approximately one half of that (2.9) under the optimal control (figure 15*a*), indicating a substantially weakened C-pillar vortex. As a result, no low-pressure region is present near the side edge of the window (figure 19). There exist two $\bar{\omega}_x^*$ concentrations behind the upper and lower edges of the base (figure 21*a*), the signatures of the legs of the two recirculation bubbles, as is evident in the time-averaged streamlines. The time-averaged streamlines in the (x, y) plane of $z^* = 0.24$ show one recirculation

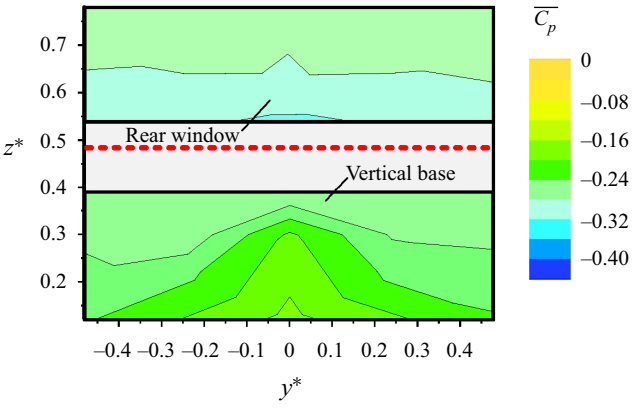

Figure 19. Distributions of $\overline{C_p}$ on the rear window and vertical base of the Ahmed body under the control law $\boldsymbol{BR_e}$ that achieves the highest η of 25.7. The red-coloured dotted line denotes the upper edge of the vertical base, while the grey area falling between the two horizontal black-coloured lines is the region where the surface pressure could not be measured due to the presence of actuators.

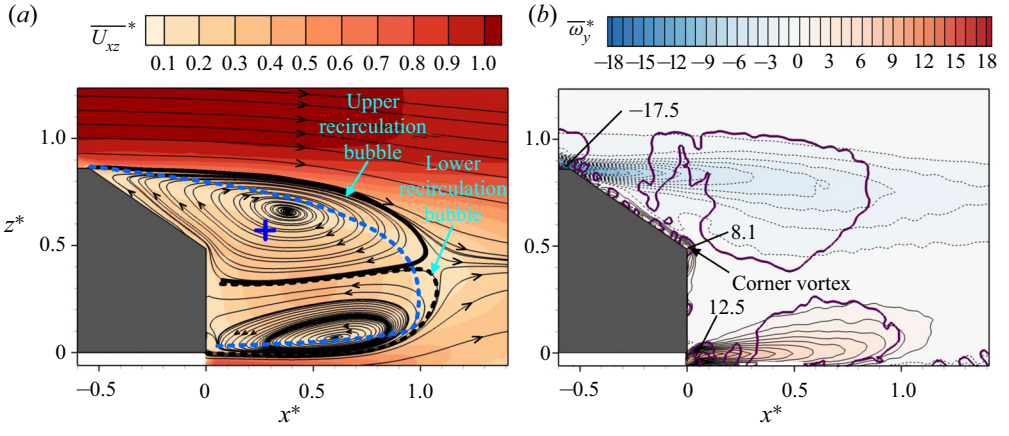

Figure 20. Time-averaged streamlines (a) superimposed with the $\overline{U_{xz}}^*$-contours, and the $\bar{\omega}_y^*$-contours (b) in the (x, z) plane of $y^* = 0$ under $\boldsymbol{BR_e}$. The blue symbol '+' in (a) denotes the focus and the thick blue broken line indicates the bubble size in the unforced flow determined from the streamlines in figure 5(a); the thick purple closed contours in (b) correspond to the time-averaged swirling strength $\overline{\lambda_{ci}^2}^* = 0.1$.

bubble behind each lateral part of the base under $\boldsymbol{BR_e}$ (figure 21b). The centre of this bubble is shifted appreciably downstream as compared with the base flow, producing an increase in $\overline{C_p}$ by 8 % near the centre of the base (figure 19). In comparison, under the optimal control, the separated shear layer from each side edge of the base is deflected inward by C_4 (figure 16d), resulting in a boat tailing effect. This effect creates a higher surface pressure recovery near the base centreline, with $\overline{C_p}$ near the base centre rising by 22 % (figure 13b), almost triple that (8 %) under $\boldsymbol{BR_e}$ (figure 19). The $\boldsymbol{BR_e}$ fails to produce this boat tailing phenomenon since its blowing strength BR^{C4} of C_4 is small, only 0.7 (cf. $BR^{C4} = 1.3$ under the optimal control).

In summary, under the most efficient control, the mechanism is completely different from that under the optimally combined actuations. The blowing ratios of BR^{C1}, BR^{C2} and BR^{C3} are reduced to no more than 15 %, and BR^{C4} and BR^{C5} drop by half, compared

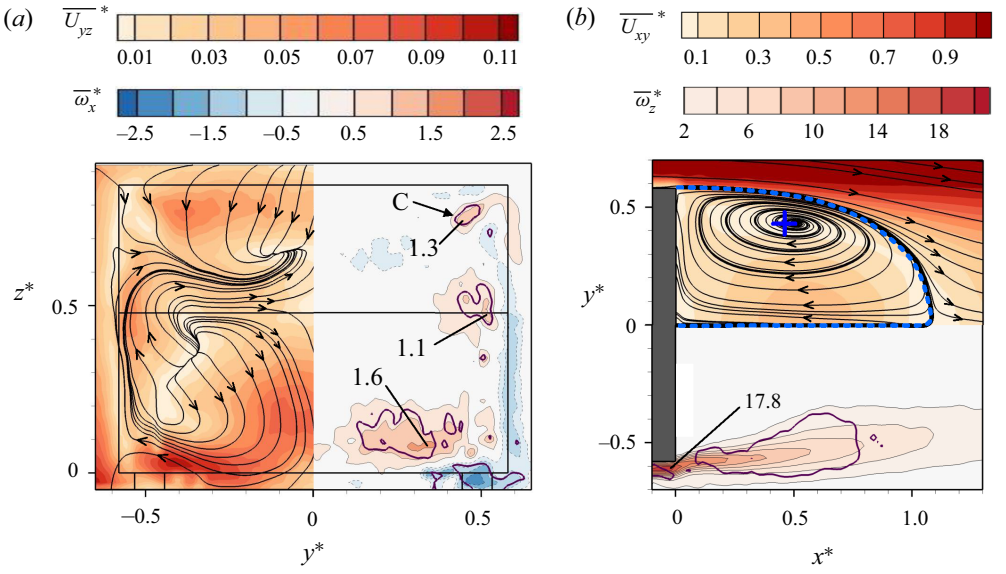

Figure 21. (*a*) Time-averaged streamlines, superimposed with the $\overline{U_{yz}}^*$-contours (left half), and $\bar{\omega}_x^*$-contours (right half) in the (y, z) plane of $x^* = 0.43$; (*b*) time-averaged streamlines, superimposed with the $\overline{U_{xy}}^*$-contours (upper half), and $\bar{\omega}_z^*$-contours (lower half) in the (x, y) plane of $z^* = 0.24$, where the blue symbol '+' denotes the focus and the thick blue broken lines indicate the bubble size in the unforced flow determined from the streamlines in figure 16(*b*). Thick purple closed contours correspond to (*a*) the time-averaged swirling strength $\overline{\lambda_{ci}^2}^* = 0.1$ or (*b*) 0.001. Flow is manipulated under $\boldsymbol{BR_e}$.

with the optimized combination, that is, the control energy is greatly reduced, resulting in $\eta = 25.7$ (c.f. $\eta = 0.13$ under the optimally combined actuations). As a result, the C-pillar vortices do not change significantly. However, the upper recirculation bubble contracts by half vertically, while the lower bubble expands, covering most part of the base (cf. the upper bubble covering almost the entire base under the optimally combined actuations, figure 14). Furthermore, both bubbles are elongated longitudinally, with their centres shifting downstream (figure 20). It is the contracted upper recirculation bubble size and the downstream shift in the centres of the two bubbles that contribute to the rise in $\langle \overline{C_p} \rangle_r$ and $\langle \overline{C_p} \rangle_b$ by 13 % and 9 %, respectively, or a *DR* of 10 %.

The present work is performed for a low-drag Ahmed body given a streamwise flow of constant velocity. Nevertheless, the obtained optimization laws may provide a valuable guidance for the *DR* of practical SUV and MPV vehicles, though more investigations are required should the laws be applicable for real road vehicles subjected to cross-winds and transient flow conditions.

5. Conclusions

A rather extensive investigation has been conducted on the active *DR* of a low-drag Ahmed body ($\varphi = 35°$) using five independently operated arrays of steady blowing jets, C_i ($i = 1, 2, \ldots, 5$), deployed around the rear window and vertical base of the body. The ACA is used for the first time to search for the best combination strategy of the five jets or actuators. Exhaustive flow measurements were performed in order to unveil the *DR* mechanisms behind the optimized controls, with either the largest *DR* or a high efficiency given a small sacrifice in *DR*. Major conclusions are drawn below.

An AI control system is developed for maximizing the *DR* of the Ahmed body with efficiency considered. The parameter search space comprises the blowing ratios of the five independent actuators. The control target is to minimize the cost J that is linked to the total drag with a penalization term related to control power input. The learning process converges after eight cycles, with 800 control laws tested. The optimal control law leads to a rise in $\Delta\langle\overline{C_p}\rangle$ by 32 % and a *DR* by 18 %, greatly exceeding the maximum *DR* (4 %) achieved in previous experiments for a low-drag Ahmed body (e.g. Jahanmiri & Abbaspour 2011). It is worth noting that the DRs obtained by individual C_i ($i = 1, 2, \ldots, 5$) are 9 %, 1 %, 2 %, 1 % and 3 %, respectively, given the same BR^{Ci} as the optimized combination. However, the *DR* achieved by their combination exceeds the summation (16 %) of individual DRs.

The control efficiency is evaluated for the five individual actuations and their combinations. The η is large for C_1, C_3 and C_5, reaching 2.6, 31.8 and 4.5, respectively, but not for C_2 and C_4, only 0.2 and 0.6, respectively. It is difficult for C_4 to manipulate the three predominant coherent structures, i.e. the separation bubble over the window, C-pillar vortices and two recirculation bubbles behind the base. On the other hand, C_2 may produce two opposite effects on *DR*, i.e. weakening the C-pillar vortices and subsequently enhancing flow separation from the window. The optimal control is associated with a small $\eta = 0.13$. With the penalization term of control power input included in the cost (3.1), we have captured solutions in the learning process of optimization, where a small sacrifice in *DR* may lead to a large increase in η, and η rises with increasing sacrifice in *DR*, e.g. reaching 3.7 and 25.7 when *DR* drops to 16 % and 10 %, respectively.

The flow modification and mechanism of the most efficient control differ markedly from their counterpart for the optimal control. Under the optimal control, the two C-pillar vortices grow significantly in strength and induce a downwash flow between them, producing flow reattachment over the window. The reattached flow interacts with the upstream and upward blowing of C_3, generating a stagnated flow region near the lower end of the window and hence a big rise (up to 287 %) in pressure in this region, which contributes most to the increase in the averaged pressure $\langle\overline{C_p}\rangle_r$ over the rear window by 72 %. Furthermore, the shear layers separated from the side edges of the base are deflected inward, creating a boat tailing effect, accounting for a rise in in the averaged pressure $\langle\overline{C_p}\rangle_b$ on the base by 4 %. The two changes in the flow structure account for the substantial *DR*. Under the most efficient control, the blowing ratios of BR^{C1}, BR^{C2} and BR^{C3} are greatly reduced, implying a large drop in the input energy. As such, there is little change with the C-pillar vortices. Nevertheless, the upper recirculation bubble shrinks substantially and the centres of the two recirculation bubbles shift downstream, resulting in increases in $\langle\overline{C_p}\rangle_r$ and $\langle\overline{C_p}\rangle_b$ by 13 % and 9 %, respectively, and hence a substantial *DR*.

Funding. Authors wish to acknowledge support given to them from NSFC through grants 11902102, 91952204, 12272114 and 12202124, and from the Research Grants Council of Shenzhen Government through grants JCYJ20190806143611025 and JCYJ20210324132816040, and CB11409006.

Declaration of interests. The authors report no conflict of interest.

Author ORCIDs.
B.F. Zhang https://orcid.org/0000-0001-8696-5169;
D.W. Fan https://orcid.org/0000-0002-2652-4414.

References

Ahmed, S.R., Ramm, R. & Faltin, G. 1984 Some salient features of the time-averaged ground vehicle wake. *Paper* 840300, pp. 1–30. Society of Automotive Engineers.

AUBRUN, S., MCNALLY, J., ALVI, F. & KOURTA, A. 2011 Separation flow control on a generic ground vehicle using steady microjet arrays. *Exp. Fluids* **51**, 1177–1187.

BARROS, D., BORÉE, J., NOACK, B.R. & SPOHN, A. 2016 Bluff body drag manipulation using pulsed jets and Coanda effect. *J. Fluid Mech.* **805**, 422–459.

BARROS, D., RUIZ, T., BORÉE, J. & NOACK, B.R. 2014 Control of a three-dimensional blunt body wake using low and high frequency pulsed jets. *Intl J. Flow Control* **6** (1), 61–74.

BIDKAR, R.A., LEBLANC, L., KULKARNI, A.J., BAHADUR, V., CECCIO, S.L. & PERLIN, M. 2014 Skin-friction drag reduction in the turbulent regime using random-textured hydrophobic surfaces. *Phys. Fluids* **26**, 085108.

BOUCINHA, V., WEBER, R. & KOURTA, A. 2011 Drag reduction of a 3D bluff body using plasma actuators. *Intl J. Aerodyn.* **1**, 262–280.

BRACKSTON, R.D., GARCÍA DE LA CRUZ, J., WYNN, A., RIGAS, G. & MORRISON, J.F. 2016 Stochastic modelling and feedback control of bistability in a turbulent bluff body wake. *J. Fluid Mech.* **802**, 726–749.

BRUNEAU, C.H., CREUSÉ, E., DEPEYRAS, D., GILLIÉRON, P. & MORTAZAVI, I. 2010 Coupling active and passive techniques to control the flow past the square back Ahmed body. *Comput. Fluids* **39** (10), 1875–1892.

BRUNEAU, C.H., CREUSÉ, E., DELPHINE, D., GILLIÉRON, P. & MORTAZAVI, I. 2011 Active procedures to control the flow past the Ahmed body with a 25° rear window. *Intl J. Aerodyn.* **1**, 299–317.

BRUNTON, S.L., NOACK, B.R. & KOUMOUTSAKOS, P. 2020 Machine learning for fluid mechanics. *Annu. Rev. Fluid Mech.* **52**, 477–508.

CHOI, H., JEON, W.P. & KIM, J. 2008 Control of flow over a bluff body. *Annu. Rev. Fluid Mech.* **40**, 113–139.

CHONG, M.S., PERRY, A.E. & CANTWELL, B.J. 1990 A general classification of three-dimensional flow fields. *Phys. Fluids* A*: Fluid Dyn.* **2**, 765–777.

COX, T. & COX, M. 2001 *Multidimensional Scaling*. Chapman & Hall.

DORIGO, M., MANIEZZO, V. & COLORNI, A. 1991 Positive feedback as a search strategy. *Tech. Rep.* 91–016. Dipartimento di Elettronica, Politecnico di Milano.

EDWIGE, S., EULALIE, Y., GILOTTE, P. & MORTAZAVI, I. 2018 Wake flow analysis and control on a 47° slant angle Ahmed body. *Intl J. Numer. Meth. Heat Fluid Flow* **28**, 1061–1079.

EVSTAFYEVA, O., MORGANS, A.S. & DALLA LONGA, L. 2017 Simulation and feedback control of the Ahmed body flow exhibiting symmetry breaking behavior. *J. Fluid Mech.* **87**, R2.

FAN, D.W., ZHANG, B.F., ZHOU, Y. & NOACK, B.R. 2020*a* Optimization and sensitivity analysis of active drag reduction of a square-back Ahmed body using machine learning control. *Phys. Fluids* **32**, 125117.

FAN, D.W., ZHOU, Y. & NOACK, B.R. 2020*b* Fast triple-parameter extremum seeking exemplified for jet control. *Exp. Fluids* **61**, 152.

GAUTIER, N., AIDER, J.L., DURIEZ, T., NOACK, B.R., SEGOND, M. & ABEL, M. 2015 Closed-loop separation control using machine learning. *J. Fluid Mech.* **770**, 424–441.

GIANNOPOULOS, A. & AIDER, J.L. 2020 Data-driven order reduction and velocity field reconstruction using neural networks: the case of a turbulent boundary layer. *Phys. Fluids* **32** (9), 095117.

GRANDEMANGE, M., MARY, A., GOHLKE, M. & CADOT, O. 2013 Effect on drag of the flow orientation at the base separation of a simplified blunt road vehicle. *Exp. Fluids* **55**, 1529.

GUILMINEAU, E. 2008 Computational study of flow around a simplified car body. *J. Wind Engng Ind. Aerodyn.* **96**, 1207–1217.

HAFFNER, Y., BORÉE, J., SPOHN, A. & CASTELAIN, T. 2020 Unsteady Coanda effect and drag reduction for a turbulent wake. *J. Fluid Mech.* **899**, A36.

HAFFNER, Y., CASTELAIN, T., BORÉE, J. & SPOHN, A. 2021 Manipulation of three-dimensional asymmetries of a turbulent wake for drag reduction. *J. Fluid Mech.* **912**, A6.

HUCHO, W.H. & SOVRAN, G. 1993 Aerodynamics of road vehicles. *Annu. Rev. Fluid Mech.* **25**, 485–537.

JAHANMIRI, M. & ABBASPOUR, M. 2011 Experimental investigation of drag reduction on Ahmed car model using a combination of active flow control methods. *Intl J. Engng Trans.* B*: Appl.* **24**, 403–410.

JOSEPH, P., AMANDOLESE, X. & AIDER, J.L. 2012 Drag reduction on the 25° slant angle Ahmed reference body using pulsed jets. *Exp. Fluids* **52**, 1169–1185.

JOSEPH, P., AMANDOLESE, X., EDOUARD, C. & AIDER, J.L. 2013 Flow control using MEMS pulsed micro-jets on the Ahmed body. *Exp. Fluids* **54**, 1442.

KAISER, E., NOACK, B.R., SPOHN, A., CATTAFESTA, L.N. & MORZYŃSKI, M. 2017 Cluster-based control of nonlinear dynamics. *Theor. Comput. Fluid Dyn.* **31**, 1579–1593.

KHAN, T.I., PAREZANOVIĆ, V., PASTUR, L. & CADOT, O. 2022 Suppression of the wake steady asymmetry of an Ahmed body by central base bleed. *Phys. Rev. Fluids* **7** (8), 083902.

KIM, D., DO, H. & CHOI, H. 2020 Drag reduction on a three-dimensional model vehicle using a wire–to–plate DBD plasma actuator. *Exp. Fluids* **61**, 135.

KOURTA, A. & LECLERC, C. 2013 Characterization of synthetic jet actuation with application to Ahmed body wake. *Sensors Actuators* A-*Phys.* **192**, 13–26.

LI, R., BARROS, D., BORÉE, J., CADOT, O., NOACK, B.R. & CORDIER, L. 2016 Feedback control of bimodal wake dynamics. *Exp. Fluids* **57**, 158.

LI, R., BORÉE, J., NOACK, B., CORDIER, L. & HARAMBAT, F. 2019 Drag reduction mechanisms of a car model at moderate yaw by bi-frequency forcing. *Phys. Rev. Fluids* **4** (3), 034604.

LI, Y., CUI, W., JIA, Q., LI, Q., YANG, Z., MORZYŃSKI, M. & NOACK, B.R. 2022 Explorative gradient method for active drag reduction of the fluidic pinball and slanted Ahmed body. *J. Fluid Mech.* **932**, A7.

LI, R., NOACK, B.R., CORDIER, L., BORÉE, J. & HARAMBAT, F. 2017 Drag reduction of a car model by linear genetic programming control. *Exp. Fluids* **58**, 103.

LIAO, T., MONTES DE OCA, M., STÜTZLE, T. & DORIGO, M. 2014 A unified ant colony optimization algorithm for continuous optimization. *Eur. J. Oper. Res.* **234**, 597–609.

LIENHART, H. & BECKER, S. 2003 Flow and turbulent structures in the wake of a simplified car model. *Paper* 2003-01-0656. Society of Automotive Engineers.

LING, J., KURZAWSKI, A. & TEMPLETON, J. 2016 Reynolds averaged turbulence modelling using deep neural networks with embedded invariance. *J. Fluid Mech.* **807**, 155–166.

LITTLEWOOD, R.P. & PASSMORE, M.A. 2012 Aerodynamic drag reduction of a simplified squareback vehicle using steady blowing. *Exp. Fluids* **53**, 519–529.

LIU, K., ZHANG, B.F. & ZHOU, Y. 2021 Correlation between drag variation and rear surface pressure of an Ahmed body. *Exp. Fluids* **62**, 124.

LORITE-DÍEZ, M., JIMÉNEZ-GONZÁLEZ, J.I., MARTÍNEZ-BAZÁN, C., CADOT, O. & PASTUR, L. 2019 Perimetric blowing at the rear of a bluff body: consequences on the wake dynamics and drag reduction. *Proc. Appl. Maths Mech.* **19** (1), e201900044.

LORITE-DÍEZ, M., JIMÉNEZ-GONZÁLEZ, J.I., PASTUR, L., CADOT, O. & MARTÍNEZ-BAZÁN, C. 2020*a* Drag reduction of three-dimensional bodies by base blowing with various gas densities. *Phys. Rev.* E **102** (1), 011101.

LORITE-DÍEZ, M., JIMÉNEZ-GONZÁLEZ, J.I., PASTUR, L., MARTÍNEZ-BAZÁN, C. & CADOT, O. 2020*b* Experimental analysis of the effect of local base blowing on three-dimensional wake modes. *J. Fluid Mech.* **883**, A53.

MCNALLY, J., MAZELLIER, N., ALVI, F. & KOURTA, A. 2019 Control of salient flow features in the wake of 25° Ahmed model using microjets. *Exp. Fluids* **60**, 7.

MEILE, W., LADINEK, T., BRENN, G., REPPENHAGEN, A. & FUCHS, A. 2016 Non-symmetric bi-stable flow around the Ahmed body. *Intl J. Heat Fluid Flow* **57**, 34–47.

METKA, M. 2013 Flow control on the Ahmed body vehicle model using fluidic oscillators. *IMECE Paper* 2013-67343.

METKA, M. & GREGORY, J.W. 2015 Drag reduction on the 25-deg Ahmed model using fluidic oscillators. *Trans. ASME J. Fluids Engng* **137**, 051108.

NARASIMHA, R. & PRASAD, S.N. 1994 Leading edge shape for flat plate boundary layer studies. *Exp. Fluids* **17** (5), 358–360.

PAREZANOVIĆ, V., CORDIER, L., SPOHN, A., DURIEZ, T., NOACK, B.R., BONNET, J.P., SEGOND, M., ABEL, M. & BRUNTON, S.L. 2016 Frequency selection by feedback control in a turbulent shear-flow. *J. Fluid Mech.* **797**, 247–283.

PARK, H., CHO, J.H., LEE, J., LEE, D.H. & KIM, K.H. 2013 Experimental study on synthetic jet array for aerodynamic drag reduction of a simplified car model. *J. Mech. Sci. Technol.* **27**, 3721–3731.

PERNOD, P., MERLEN, A., TALBI, A., PREOBRAZHENSKY, V., VIARD, R., GIMENO, L. & DUCLOUX, O. 2011 IEMN/LEMAC magneto-mechanical microjets and micro-hotwires and aerodynamic active flow control. *Intl J. Aerodyn.* **1** (3/4), 243–261.

PLUMEJEAU, B., DELPRAT, S., KEIRSBULCK, L., LIPPERT, M. & ABASSI, W. 2019 Ultra-local model-based control of the square-back Ahmed body wake flow. *Phys. Fluids* **31** (8), 085103.

RAIBAUDO, C., ZHONG, P., NOACK, B.R. & MARTINUZZI, R.J. 2020 Machine learning strategies applied to the control of a fluidic pinball. *Phys. Fluids* **32**, 015108.

REN, F., HU, H.B. & TANG, H. 2020 Active flow control using machine learning: a brief review. *J. Hydrodyn.* **32** (2), 247–253.

SCIACCHITANO, A., WIENEKE, B. & SCARANO, F. 2013 PIV uncertainty quantification by image matching. *Meas. Sci. Technol.* **24**, 045302.

SHADMANI, S., MOUSAVI NAINIYAN, S.M., GHASEMIASL, R., MIRZAEI, M. & POURYOUSSEFI, S.G. 2018 Experimental study of flow control over an Ahmed body using plasma actuator. *Mech. Mech. Engng* **22** (1), 239–251.

SOCHA, K. & DORIGO, M. 2008 Ant colony optimization for continuous domains. *Eur. J. Oper. Res.* **185**, 1155–1173.

TOUNSI, N., MESTIRI, R., KEIRSBULCK, L., OUALLI, H., HANCHI, S. & ALOUI, F. 2016 Experimental study of flow control on bluff body using piezoelectric actuators. *J. Appl. Fluid Mech.* **9** (2), 827–838.

WANG, B.X., YANG, Z.G. & ZHU, H. 2019 Drag reduction on the 25° Ahmed body using a new zero-net-mass-flux. *Theor. Comput. Fluid Dyn.* **3**, 1–21.

WANG, X.W., ZHOU, Y., PIN, Y.F. & CHAN, T.L. 2013 Turbulent near wake of an Ahmed vehicle model. *Exp. Fluids* **54**, 1490.

WASSEN, E. & THIELE, F. 2010 Simulation of active separation control on a generic vehicle. *AIAA Paper* 2010-4702.

ZHANG, B.F., LIU, K., ZHOU, Y., TO, S. & TU, J.Y. 2018 Active drag reduction of a high-drag Ahmed body based on steady blowing. *J. Fluid Mech.* **856**, 351–396.

ZHANG, B.F., ZHOU, Y. & TO, S. 2015 Unsteady flow structures around a high-drag Ahmed body. *J. Fluid Mech.* **777**, 291–326.

ZHOU, J., ADRIAN, R.J., BALACHANDAR, S. & KENDALL, T.M. 1999 Mechanisms for generating coherent packets of hairpin vortices in channel flow. *J. Fluid Mech.* **387**, 353–396.

ZHOU, Y. & ANTONIA, R.A. 1994 Critical points in a turbulent near-wake. *J. Fluid Mech.* **275**, 59–81.

ZHOU, Y., DU, C., MI, J. & WANG, X.W. 2012 Turbulent round jet control using two steady mini-jets. *AIAA J.* **50**, 736–740.

ZHOU, Y., FAN, D., ZHANG, B.F., LI, R. & NOACK, B.R. 2020 Artificial intelligence control of a turbulent jet. *J. Fluid Mech.* **897**, A27.

ZHOU, Y. & ZHANG, B.F. 2021 Recent advances in wake dynamics and active drag reduction of simple automotive bodies. *Appl. Mech. Rev.* **73**, 060801.